2020

Crystalline Structure And Phase Development In Tio2-Zro2 Ceramic Nanofibers From Electrospun Precursors

Lindsey Elizabeth Motlow
University of Alabama at Birmingham

CRYSTALLINE STRUCTURE AND PHASE DEVELOPMENT IN TiO_2-ZrO_2 CERAMIC NANOFIBERS FROM ELECTROSPUN PRECURSORS

by

Lindsey Motlow

Andrei Stanishevsky, CHAIR
Kannatassen Appavoo
Cheng-Chien Chen

A THESIS

Submitted to the graduate faculty of The University of Alabama at Birmingham,
in partial fulfillment of the requirements for the degree of
Master of Science

BIRMINGHAM, ALABAMA

2020

CRYSTALLINE STRUCTURE AND PHASE DEVELOPMENT IN TiO_2-ZrO_2 CERAMIC NANOFIBERS FROM ELECTROSPUN PRECURSORS

LINDSEY MOTLOW

PHYSICS

ABSTRACT

This study focuses on crystallization and phase relations for various molar ratios of the free-surface alternating current electrospun nanofibrous composite material, Zirconium Titanate. Both ZrO_2 and TiO_2 based ceramic nanomaterials have been of increasing interest in recent years for applications in pollutants abatement, water splitting, optical and memory devices, humidity sensors, high temperature pigments, and biomaterials. The mixed TiO_2-ZrO_2 system is a semiconducting oxide and photoactive system that has shown very promising properties in these applications, depending on structure and phase composition. Molar ratios of TiO_2/ZrO_2 from 0.1:0.9 to 0.8:0.2 were tested in this study. The precursor based fibrous materials were fabricated at a rate that corresponded to a 2.4-8.4 g/h yield of TiO_2/ZrO_2 ceramic nanofibers. All systems crystallized above 600°C and formed ceramic nanofibers with 250-350 nm mean fiber diameters and nanocrystalline structures which were stable up to 1200°C, depending on the composition. Stable zirconium titanate (srilankite) single phase nanofibers formed when the TiO_2/ZrO_2 molar ratio was between 0.5:0.5 and 0.6:0.4. The TiO_2/ZrO_2 compositions with up to 30 mol% were single phase tetragonal zirconia, stable up to 1000°C, whereas mixed srilankite/rutile nanofibers formed at 0.8:0.2 TiO_2/ZrO_2 molar ratio.

Key words**:** Electrospinning, nanofibers, photocatalysis, phase diagram, crystallization, Zirconium Titanate

DEDICATION

This is dedicated to Elijah. My interminable motivation, my greatest challenge, my check and my balance, the weight against whom I appraise all decision and risk, my light in every seemingly inescapable dark moment, my son.

ACKNOWLEDGEMENTS

I thank my mentor and biggest supporter, Dr. Andrei Stanishevsky, who gave me a chance and, more importantly, a path to return to this program and jump into an exciting and fast-tracked field of experimental research. Dr. Stanishevsky has supported encouraged, and advocated for me far beyond what was required and has been effortlessly patient throughout every stage of my research progress. His mentorship, amusing tales, and contagious sense of excitement and passion for this field have been invaluable.

I thank all the members of Dr. Stanishevsky's lab including Anthony Brayer, Sara Nealy, Micah Armstrong, Courtney Severino, and Amanda Kennell for their constant support and collaborative efforts in my research progress. Without them this work would have been impossible.

I thank Dr. Ryoichi Kawai for his irreplaceable patience, guidance and mentorship in my first few tumultuous years in the program. His inherent passion, the high bar he set for performance, and his ability to articulate difficult concepts into intuitive and accessible terms has influenced me across the board and will stay with me for the rest of my life in my personal approach to learning new material and developing new ideas, my teaching philosophy, and my resilience in the face of difficulties.

I thank the entire staff and administration of the Department of Physics for my financial support, the opportunity to continue in my pursuit of higher education, and for the trust year after year.

TABLE OF CONTENTS

Page

LIST OF FIGURES

1. INTRODUCTION

1.1 Transition Metal Oxides: ZrO_2 and TiO_2

Inorganic-inorganic nanomaterial composites have been of great interest in recent years due to their broad range of applications across the board including, but not limited to, the environmental industry, materials science, telecommunications, energy industry, and medical field. Arguably the most interesting feature of these structures is their effectivity as photocatalysts. The most common inorganic-inorganic structures in modern photocatalytic research are Titanium oxide based nanocomposites. (1-7)

TiO_2, "titania," is a naturally formed oxide of Titanium, common in a good number of metamorphic or igneous rocks or even soils. These naturally occurring materials containing TiO_2 benefit from the weather resistant and dense properties of the material. Titania is commonly used for a wide range of applications in the status quo. It can be used in photochemical energy conversion processes, water splitting, photocatalysis/organic pollution removal, the production of surfactants, white pigments and insecticides, electrical ceramics, conductors, telecommunication, microelectronics, and chemical intermediates. (8-13) The most abundant phases of TiO_2 are rutile, anatase, and brookite (fig. 1). The most common crystalline form of TiO_2 for photocatalytic applications is anatase, however rutile and mixed phase are also of interest for other applications. (14-22)

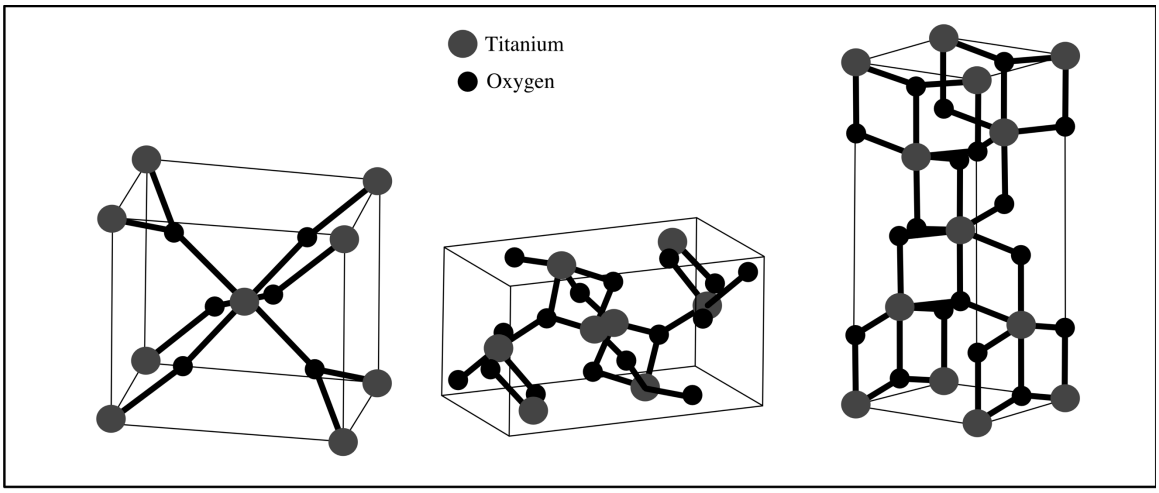

Figure 1. Crystalline states of TiO_2. Large circles are Ti atoms and small circles are O atoms

TiO_2 has a crystal lattice easily disturbed by lack of purity. Specifically, as a photocatalyst, TiO_2 is incredibly attractive due to the ease of obtainability, nontoxicity, and affordability, but there are some disadvantages. TiO_2 is a high-energy band semiconductor, with $Eg \approx 3.2$ eV. This fact means that it would be nearly impossible for sunlight radiation to cause photoreaction. TiO_2 also has a low quantum yield rate and photo-oxidation rate and weak reduction potential of photoexcited electrons. (23-24) Moreover, titanium dioxide based photocatalysts have also proven to have incredibly poor mechanical properties (25).

ZrO_2, "zirconia," is often called the "all-purpose construction material" (26-28) due to its incredibly high resistance to crack propagation, the ability to conduct oxygen ions, high thermal expansion similar to many types of steel, chemical/dimensional stability, alkali resistance, non-toxicity, biocompatibility and extraordinary thermal insulation/low thermal conductivity. This high-strength material produces components that are more

expensive than those made of alumina ceramics, but are widely used in applications such as in tools for wire forming, auxiliaries in welding processes, materials in the dental industry, insulation, and tools for oxygen measurement. Zirconia based bioceramics are incredibly popular as a class of biomaterial due to the abovementioned properties. (29-30) Fibrous and nano-scale form of this material has been shown to be potentially useful for load-bearing biomedical applications such as bone tissue engineering and dental industry materials due to the necessary high surface area and strength.

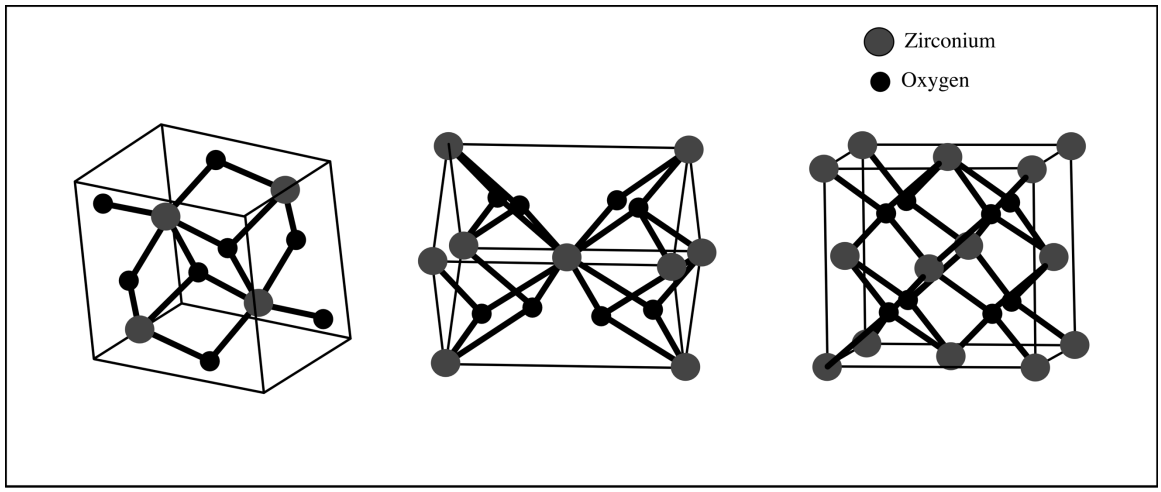

Figure 2. Crystalline states of ZrO_2. Large circles are Zr atoms and small circles are O atoms

1.2 The System TiO_2-ZrO_2

There is a standing need for a photoactive solid that can go beyond traditional Titanium Dioxide materials while implementing TiO_2 positive properties. Thus, research has recently moved into the study of composite materials within the ZrO_2-TiO_2 system with

various molar combinations of individual oxides, ranging from ZrO_2-doped titania through a stoichiometric zirconium titanate ($ZrTiO_4$) to TiO_2-doped zirconia. Both zirconia and titania are n-type semiconductors and are in the same group of elements. (1). The TiO_2-ZrO_2 system, like titania, is a semiconducting oxide and photoactive system and has an analogous structure to TiO_2 polymorphs but with a wider band gap and other unique properties such as enhanced photocatalytic performance, thermal stability, and surface properties as well as appreciably stronger mechanical properties (31). There are many ways to consider the combination system that open up completely new types of materials with novel properties. The four systems of interest in this study are Zr-doped TiO_2, Ti-doped ZrO_2(less than 5% molar), solid solution and mixed-phase non-stoichiometric TiO_2-ZrO_2 (with 10%-40% molar ratio of either oxide) and in the middle ground, stoichiometric $ZrTiO_4$. Literature has shown that crystalline structure, surface morphology, phase, and chemical composition all strongly affect potential performance of these structures in applications of interest. (1-6) It is therefore important to understand the crystallization and phase development of this composite material for various production methods and compositions in order to optimize its use in the applications of interest.

Experimental studies of the TiO_2-ZrO_2 system have typically been accomplished by production methods such as high temperature (1400°C and above) sintering of oxides/carbonates due to slow kinetics of the reaction. Melt quenching is not ideal with this combination of materials and prevents any homogeneous mixing. Limitations of producing this composite by sintering of oxides can be linked to the incredibly slow diffusion of solid state reaction and immiscibility of the two materials of interest. Between ~.3 and ~.45 molar fraction TiO_2 and ~.6 and ~.9 molar fraction TiO_2 there are immiscibility gaps upon

calcination conditions. Unfortunately, this leads to inhomogeneity in the atomic distribution in the final material, making it less than ideal for use in application. (32-34) To obtain ordered TiO_2-ZrO_2, methods have been limited due to the tendency of crack development during ordering transition during the slow cooling process.

The sol-gel method is also known to give an uncertain equilibrium state and result in difficulty identifying composition. (35-44) Most sol-gel synthesis studies currently focus on producing TiO_2-ZrO_2 powders with high surface energies. (45-47) In order to obtain a consistent and distinct stoichiometry of resultant materials for various compositions, purely sol gel methods involve incredibly complex optimization procedures and conditions. They do however also tend to be able to produce materials devoid of organics after annealing and highly porous microstructures with reasonably small grain sizes. (34)

The limit of solubility of TiO_2 in ZrO_2 has not been explored for sol gel produced materials or at low temperatures.

1.3 TiO_2-ZrO_2 Nanofibers

Seeing as the most prominent application of interest for TiO_2 systems is arguably photocatalysis, the main interest of modern research in the area is increasing this function by any experimental means. In addition to chemical and crystalline modification, the method of production plays an incredibly important role in enhancing properties of the material. Traditional wet chemical methods such as co-precipitation, hydrothermal, and sol gel have been used to produce Zr-doped TiO_2 nanomaterials and vice versa, but they are usually found in the form of nanoparticles. (48-49) Materials in this form are not only limited by their complex, low-output, inefficient and often unsustainable production

methods, but also in their physical nature. Nanoparticles have a major tendency to disperse in water, which makes it almost impossible to recycle them, one of the critical issues for a photocatalyst in potential applications. Researchers have attempted to seed these photocatalytic nanoparticles onto supporting materials or substrates to avoid aggregation and make it possible to reclaim and recycle them, however this process makes the already unsustainable, low output and complex means of production even more complex and majorly reduces the photocatalytic efficiency of the system as a whole due to rendering the seeded nanoparticles inaccessible. (50-53)

Nanofibers have proven to be a great alternative to reduce many of the problems that nanoparticles face. As photocatalysts, Nanofibers have demonstrated a significantly higher efficiency than nanoparticles. (54-58) Electrospinning results in a scaffold-like, high surface area, highly porous structure that additionally can prevent aggregation and provide more contact points for enhanced photocatalytic activity. (59)

Traditionally nanofibers are produced by direct current (DC) electrospinning from polymer-based precursor solutions. Electrospinning is a surprisingly simple method with a very complex underlying physics. The general concept developed in the late 1900's when Charles V. Boys experimentally drew fibers from a viscoelastic liquid due to an imposed electric potential difference. (60) Traditional DC electrospinning involves a few main components: a direct current (DC) high voltage power supply, a syringe pump, a spinneret, and a conductive collector (fig. 3). Upon the influence of the static electric field on the solution, released as a droplet by the capillary needle, electrostatic repulsion between like-signed surface charges causes a deformation in the surface topology resulting in a structure called a "Taylor cone." After the Taylor cone is formed, a charged liquid jet eventually

shoots out of the end of the cone forming fibers that whip due to bending instabilities, causing finer and finer fibers that solidify in air and are deposited on the collector. The spinneret or capillary needle functions as an initial electrode and fibers are collected on the conductive collector, operating as an oppositely charged electrode.

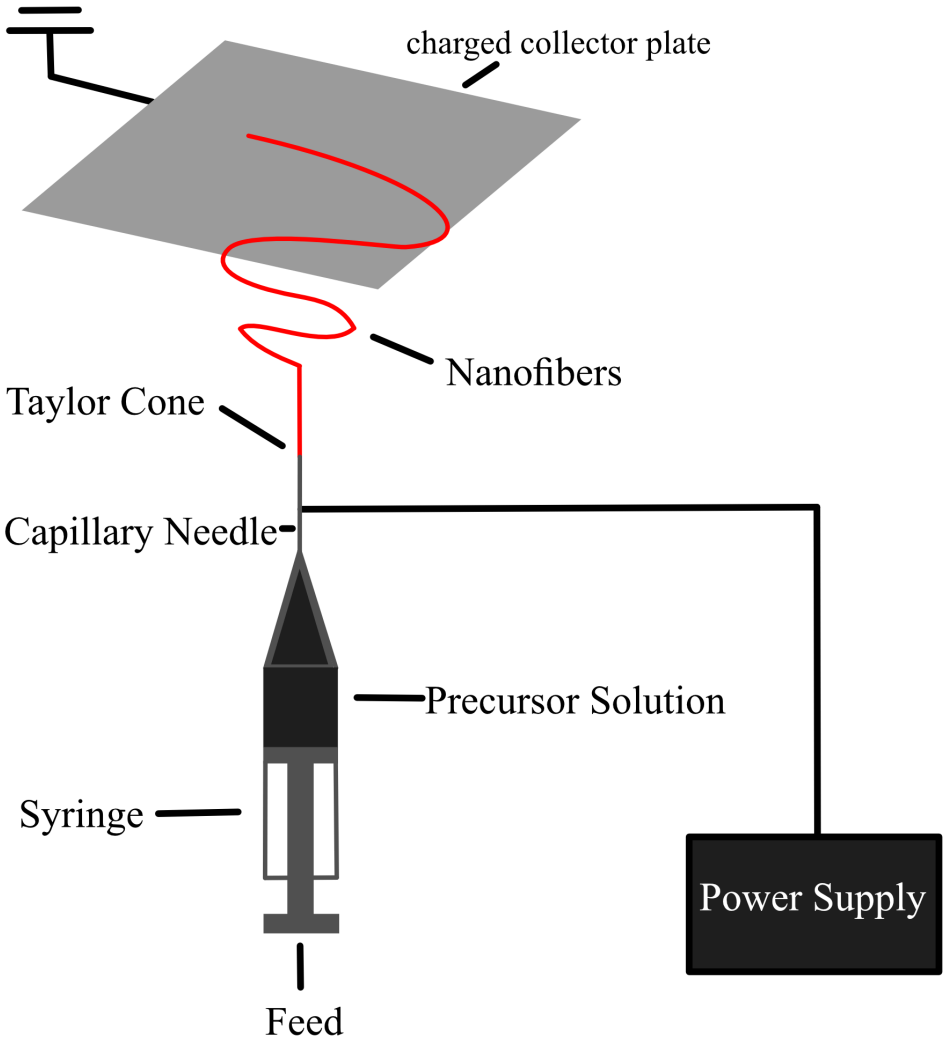

Figure 3. Schematic of a DC electrospinning device

Unfortunately, capillary needle DC electrospinning results in very low flow rates and subsequent low productivity, majorly limiting its use in practical applications or industry. Free-surface DC electrospinning, while improving the productivity, suffers from

a very high voltage requirement and electrode shape related limitations. Recently, Alternating Current (AC) electrospinning has been used without a capillary needle and instead a "free surface" resulting in an incredibly high throughput and high-density method of fiber production that works without a charged collector due to greatly enhanced ionic wind phenomena controlling loft. Fibers resulting from AC electrospinning also contain almost no electric charge during propagation (61-62). AC electrospinning typically requires a different design and different precursor requirements than DC electrospinning.

Generally, electrospinning combines the sol gel chemistry of precursor preparation from metal salts of interest with the application of an electric field in the fiber production process. Once fibers are produced, they are annealed. The annealed and cooled samples are then subject to testing or desired application.

One particular recent study in Zr-doped TiO_2 Nanofibrous membranes produced by DC electrospinning (63) found that integration of Zirconium lowered the breaking tendency of TiO_2 nanofibers, especially at higher temperatures, reduced surface defects, and successfully constrained grain growth. TiO_2 fibers doped with Zr also showed significantly enhanced photocatalytic ability in methylene blue degradation.

1.4 TiO_2-ZrO_2 Phase Diagram

There are several different phase diagrams of the TiO_2-ZrO_2 system that have been suggested due to data obtained from various production methods based on coarse-grained metal oxide powders. (32, 39, 43, 64-66) Fig. 4 fits data found by initial studies from the 60's and 70's by Noguchi, Ono, and Shevchenko. (65) It has been found in these traditional studies that Ti^{4+} is approximately soluble up to 16 mol% in tetragonal zirconia, and that

rutile Titania is able to dissolve a similar amount of Zirconia. Clearly according to figures 4 and 5, there is a notable difference in the character of the region of intermediate phase as well as stability and equilibrium configuration at lower temperatures. Many modern phase diagrams for the TiO_2-ZrO_2 system were obtained by implementing fluxes such as CuO and Li_2MoO_4 to get to equilibrium states in spite of slow kinetics. (40-41)

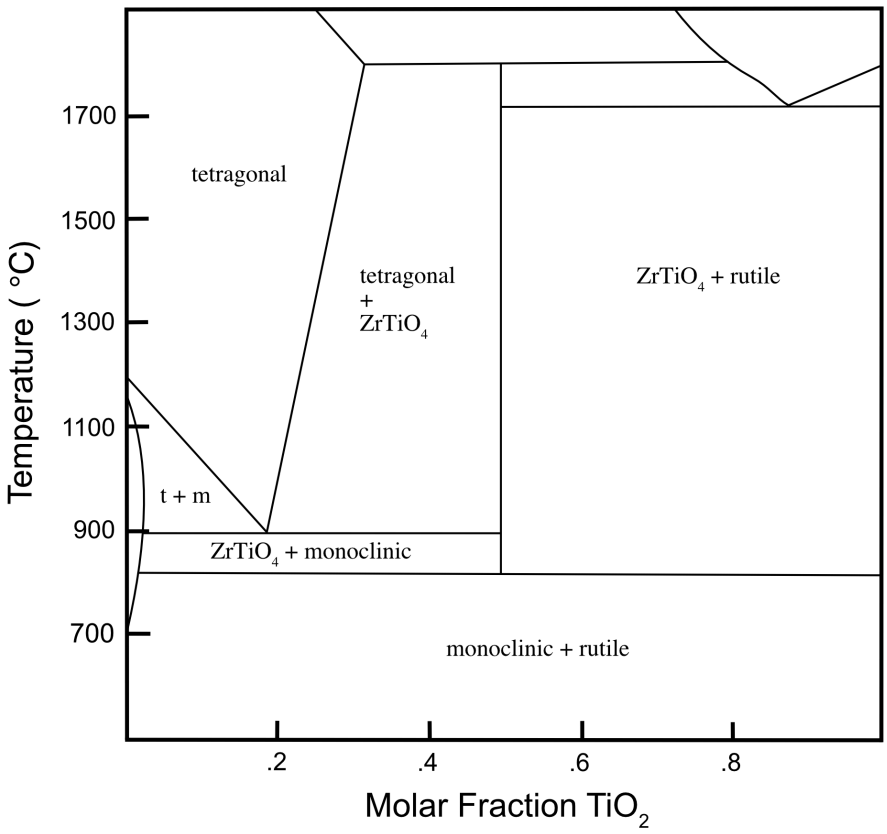

Figure 4. TiO_2-ZrO_2 classical phase diagram adapted from Noguchi, Ono, and Shevchenko (1967) (63)

In the classical phase diagram, the initial mixture of oxides as monoclinic and rutile remains stable to at least 800°C. The formation of $ZrTiO_4$ and a second phase (either rutile

TiO_2 or monoclinic ZrO_2) is observed at 800°C in the entire range of compositions, except for a small region with a few mol% of TiO_2 doping of ZrO_2. Tetragonal ZrO_2 forms above 900°C. Between ~.03 and .2 molar fraction TiO_2 there is a region where both tetragonal and monoclinic Zirconia phases exist. Stoichiometric zirconium titanate and tetragonal zirconia phase form for the range of compositions between ~.2 and .5 molar fraction TiO_2 and remains stable until above 1700°C. At higher temperatures and higher molar fraction TiO_2 there is a mixture of liquid and precipitated TiO_2.

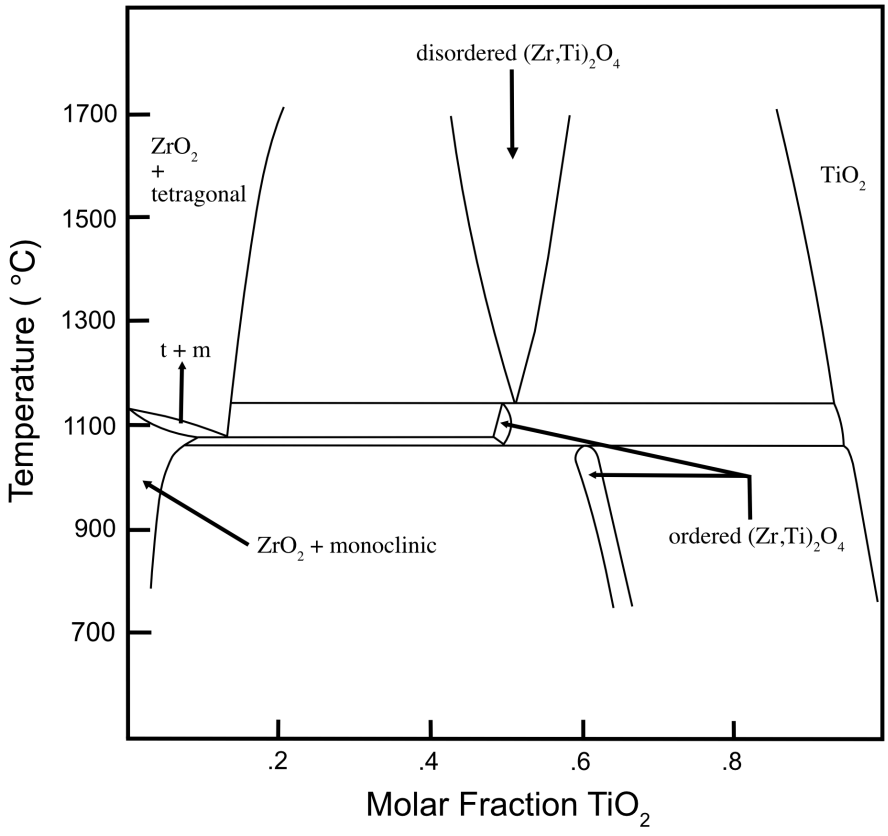

Figure 5. TiO_2-ZrO_2 phase diagram produced from data taken at atmospheric pressure from production methods of high temperature sintering from oxides and high-pressure synthesis of ordered phase directly from oxides. (43).

1.5 Goals

This system's phase diagram is of interest for the many different possible crystalline states for varying temperatures and relative concentrations. Traditionally these phase diagrams have been established using coarse powders produced by high temperature sintering methods, so it is incredibly interesting to see phase evolution for electrospun fibers in comparison, especially in a lower temperature range. Equilibrium conditions and well-crystallized TiO_2-ZrO_2 are historically very difficult to obtain below ~1200°C, so it has been challenging to illuminate true, stable phase relations in the lower temperature regime. Summarizing the material discussed above, current methods of production such as high temperature sintering of oxide powders, sol gel, melts, and DC electrospinning all come with their fair share of problems including lack of homogeneity, expense or complexity of production, low throughput, and immiscibility regimes. The goals of this study are to:

- Develop and explore a process for high throughput production of Titania and Zirconia based composite nanofibers by optimizing preparation of an accurate set of nanofibrous compositions of $Zr_xTi_{(2-x)}O_4$ through sol gel and free surface AC electrospinning techniques.
- Investigate textural properties and chemical composition of obtained materials.
- Investigate thermal stability and optimize thermal processing procedures of obtained materials.
- Investigate and identify crystalline structure and phase composition of obtained materials.

2. METHODS

2.1 Modified Sol Gel Procedure for Precursor Preparation

Titanium(IV) n-Butoxide ($Ti(OBu)_4$, 99+%), Zirconium propoxide ($Zr(OPr)_4$, 70% solution in propanol), polyvinylpyrrolidone (PVP, Mw=1,300,000), hydroxypropyl cellulose (HPC, Mw=100,000) and glacial acetic acid (AA, Reagent grade) supplied by Alfa Aesar, and ethanol (200 Proof, Decon Labs, Inc) were used to prepare the ZrO_2-TiO_2 precursor solutions. In a typical procedure, the $Ti(OBu)_4$ and $Zr(OPr)_4$ were combined with ethanol and acetic acid in a dry box (25±5% RH), and this precursor component was added to the 10 wt% solution of 1.0/1.0 mass ratio PVP/HPC polymer blend in ethanol. The amount of ethanol in each precursor was adjusted to maintain ~5 wt% polymer concentration. The ratios for each molar composition of Zr to Ti alkoxides were: 5.9:0.5, 4.8:1.5, 3.6:2.7, and 1.6:4.8. The $Ti(OBu)_4$ + $Zr(OPr)_4$ to polymer mass ratio ([$Ti(OBu)_4$/ $Zr(OPr)_4$]:PVP/HPC) was set as ~1.5 grams of the resulting oxide per one gram of polymer carrier. The precursors were stirred for up to 24 h using a magnetic stirrer and kept in sealed HDPE bottles at normal laboratory conditions (21±1 °C and 42±5% RH). All precursors were stable for at least six months

2.2 Electrospinning of Nanofibers

Alternating field electrospinning (AFES) of nanofibers was performed on a free surface AC electrospinning machine at UAB. (fig 6) This particular apparatus functions at voltages up to 40 kV rms at 60 Hz. The diameter of the free surface, shallow “dish” electrode was 25mm, and the precursor solution for each composition was dispensed

through the base at a flow rate of that corresponded to the rate of the formation of the fibrous flow. Fibers lofted and flowed upward to either a stationary mesh or rotating cylindrical collector due to ionic wind phenomena.

In AFES, a virtual electrode forms in an ionized "plasma region" where momentum transfer between moving ions generates "ionic" or "corona" wind. This begins as a pulsating action in the layer of liquid when AC field is applied that then becomes a mechanical oscillation of the entire top layer of precursor and formation of a pattern of protrusions at the liquid surface due to Faraday instabilities. Multiple Taylor cones, nonlinear charge induced surface deformities, then form from which nanoscale fibrous jets subsequently shoot and dry mid loft. Localized corona discharges can be formed due to both DC and AC fields. (67) Corona/ionic wind occurs when the ions produced by corona discharge due to a strong electric field are accelerated by a resulting electric force. This acceleration then induces a collisional momentum transfer phenomena that causes the surrounding neutral gas to move. (68-69) Drews, et al, experimentally and computationally studied Corona wind phenomena from both DC and AC sources and determined that the spatial distribution of the driving electrohydrodynamic force, based on ionization, ion transport, and recombination, is directly related to frequency, to some limit, so in AC the driving electric force stays localized near the electrode. This is the case in the experimental setup used in present experiments. This time-averaged electric force directly depends on the field between the electrode and the virtual electrode formed in the region. In AC as opposed to DC, Drews found that corona generated ions move due to the electric field and recombine after a distance δ. The force driving electric winds (1) must be entered into the

Navier Stokes equations which apply Newton's second law to fluid motion and describe the stress in a fluid as a sum of a pressure term and some diffusing viscous term.

$$\boldsymbol{f_e}(\boldsymbol{x}, t) = \rho_e \boldsymbol{E} \quad (1)$$

Here ρ_e is mobile charge density of electrons/ions. There is currently no full computational model for AC electrospinning, but the phenomena can be generally described by conservation of momentum, conservation of mass and the Navier Stokes equations describing fluid motion. In the case of AC electrospinning one can also have the complexity added of variables such as temperature and pressure gradients, evaporation of solvent, and mass transfer (70-77).

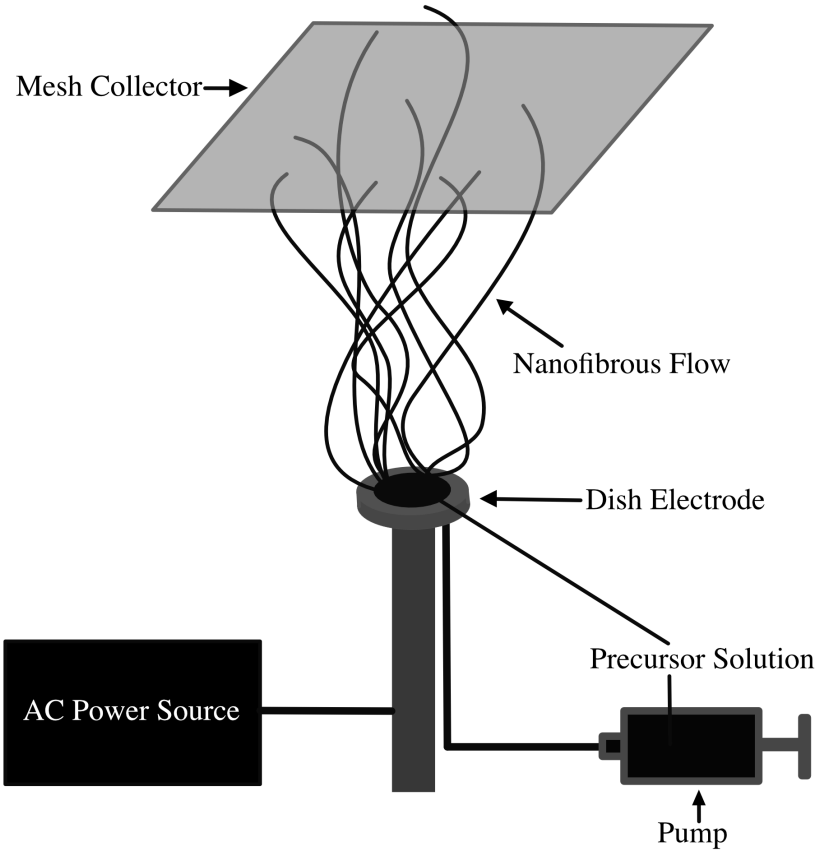

Figure 6. Schematic of an alternating field electrospinning device

Precursor spinnability and optimal electric field magnitude as well as collector height were determined by loading initial small samples onto the electrode and testing formation of stable fiber flow using a plastic wand as a rough collecting device.

Fibers were separately collected on a polytetrafluoroethylene (PTFE) plastic mesh grid (fig 7) and a rotating sheet-collecting cylinder (fig 8) placed ~44 cm above the electrode. Rotations of the sheet collector were directly monitored to assure a rotation rate compatible with the fibrous flow speed (~ 1 m/s). Temperature and humidity were monitored to be ~20°C and ~35% during all spinning sessions, with a voltage of ~30 kV rms. Fibers collected via rotating sheet collector formed roughly aligned sheets approximately 1cm thick while randomly aligned fibers collected on the mesh formed a 4-8 cm thick layer.

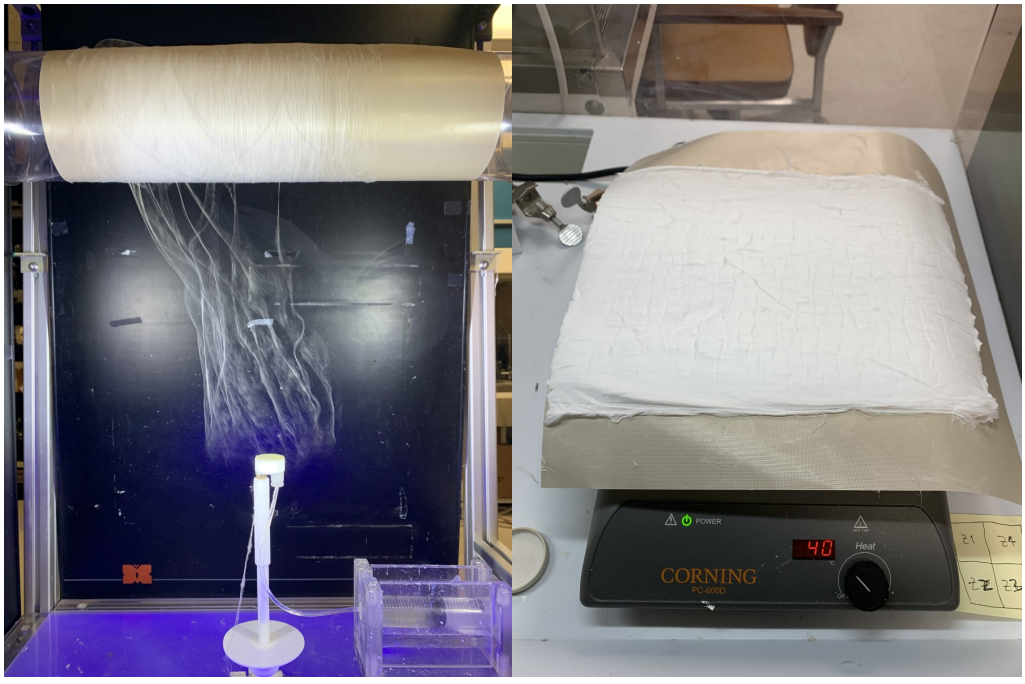

Figure 7. Fibers produced from Alternating Field electrospinning device, collected as a sheet on rotating collector.

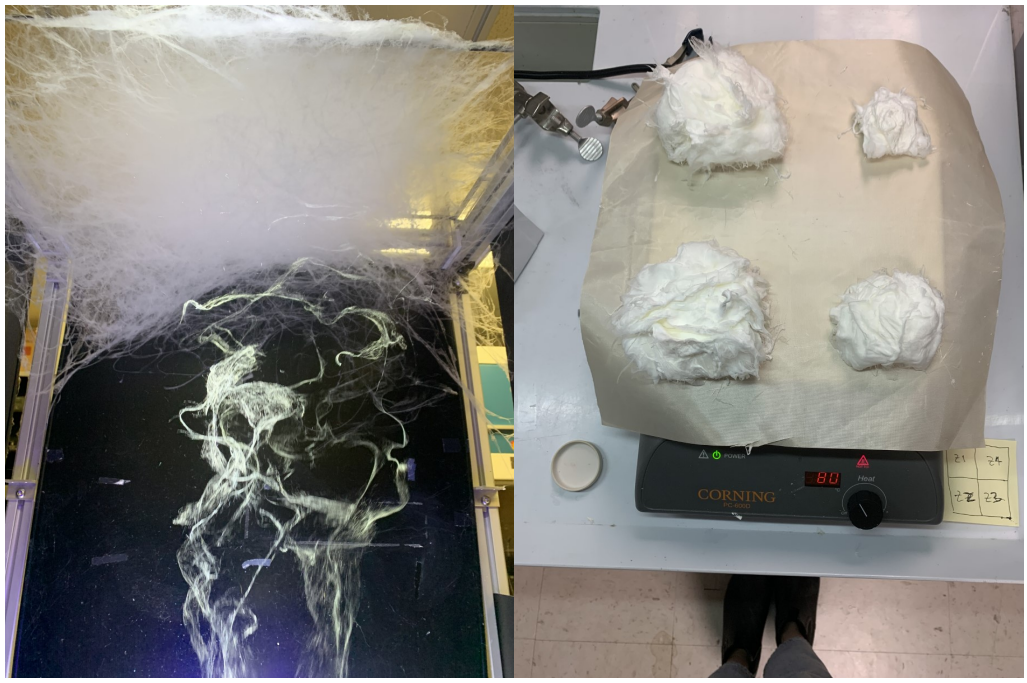

Figure 8. Fibers produced from Alternating Field electrospinning device, collected in random orientation on a mesh collector.

2.3 Thermal Processing and TGA Analysis

After the AFES process, fibers were removed and samples were placed on a hotplate at 60°C for initial drying and removal of residual solvent. These initially dried samples were then placed into ceramic crucibles or on plates and placed in a Fisher Scientific programmable furnace, heated at a rate of 2.5°C/min and annealed for two hours at temperatures of 600°C, 800°C, 1000°C, or 1200°C.

Thermogravimetric Analysis (TGA) combined with Secondary Ion Mass Spectroscopy (SIMS) analysis system was utilized to optimize the thermal processing procesure and understand the decomposition process of precursor fibers. The TGA/SIMS analysis included simultaneous recordings of thermogravimetric (TG), differential thermal

analysis (DTA) and differential thermogravimetric (DTG) curves, and it was performed using TG/DTA-SETSYS-16/18 (SETARAM, France) instrument coupled through a heated capillary adapter to a quadrupole mass spectrometer (QMS-422 ThermoStar from Balzers Instruments, 100 amu, 70 eV electron impact ionization) to monitor principal volatile species produced during the pyrolysis of precursor fibers. The samples were placed into the alumina crucibles and the mass of the samples varied between 7 and 12 mg. The TGA–DTA and ion mass spectra were recorded in air (flow rate 50 mL/min) at temperatures ranging from 20 to 900 °C with heating rate of 10 °C/min. Ion mass spectroscopy data was processed using the Quadstar 422 software.

2.3.1 Thermogravimetric Analysis

One common method of thermal processing, especially in the study of nanomaterials, is thermogravimetry. This branch of thermal analysis studies the change in weight of a material of interest as a function of either time or temperature as the material is exposed to a controlled cooling or heating environment. Thermogravimetry can be used to recognize events including oxidation, reduction, absorption, adsorption, desorption, vaporization, sublimation, phase transition, and decomposition. (79)

In a most general sense the TGA device is comprised of a dish supported by a precision balance, all within a furnace. During the experiment, this entire unit is heated or cooled and the temperature is monitored. The mass of the sample is taken throughout the entire experiment and data is graphed as a function of time. Mass loss or gain due to heating or cooling can be due to a number of physical phenomena as mentioned above, but analysis of specific TGA curves can identify what specifically is happening in the material

such as changes in sample composition, thermal stability, and kinetic parameters of chemical reactions. First one has to understand all important information about the sample, so understanding the physical chemistry of decomposition for all components is very important. Understanding this physical chemistry can allow for calculation of important information about things such as purity of the original sample. All reasons for weight change in TGA are kinetic processes. This means that the curves from TGA are not "fingerprint" as in XRD. All experimental parameters can affect shape and transition temperatures in resultant TGA curves. Reasons for weight loss in a TGA sample can be from decomposition (chemical bond breaking), reduction (sample interaction due to reducing atmosphere), desorption, or evaporation (volatile compound loss due to increased temperature). Reasons for weight gain in the sample can be from absorption/adsorption or oxidation (sample interaction due to oxidizing atmosphere.) (80)

2.3.2 Differential Thermal Analysis

In Differential thermal analysis, temperature difference between a material of interest and some reference is always measured as a function of temperature. Interestingly, change in mass is not required to get interesting information out of the sample material, and data is used to determine melting points, transition temperatures, and reaction temperatures. (81-83)

In DTA the sample material and some inert reference are put through equal thermal cycles; temperatures and temperature profiles of each material are measured over time by thermocouples over the thermal cycle's heating and cooling schedule. Symmetric arrangement is key. The difference in temperature profiles of each material identifies

transition due to energy change associated with some physical or chemical phenomenon. This is critical, for example in phase transitions. When a sample undergoes a phase transition such as melting, it will show a clear lag in temperature in the DTA curve due to energy absorption for that kinetic molecular phenomenon to take place. Curves can show endothermic (heat absorbing) and exothermic (heat releasing) peaks. The area under any DTA peak is actually the change in enthalpy. (81)

$$\Delta H = \Delta U + p\Delta V \quad (2)$$

This change in enthalpy(ΔH) is equivalent to the change in internal energy of the material (ΔU) and the pressure-volume work done by the material on the surroundings (pΔV).

Combining DTA and TGA can be extremely beneficial. TGA only measures changes due to loss in mass in a sample and DTA additionally catalogs changes without mass loss such as melting, glass transition, and crystalline structure change.

2.4 Textural Analysis and SEM

Several textural properties (surface morphology, fiber diameter, size distribution) were analyzed using scanning electron microscopy (SEM) in secondary electron mode. Elemental chemical composition was obtained using energy dispersive spectroscopy (EDS). The SEM model used was an FEI Quanta 650 FEG. Samples were sputter coated with a ~3 nm thick layer of Gold-palladium (AuPd) in order to reduce electric charge throughout the imaging process. The electron beam spot size used was 3.5 μm.

Processing of final images to determine fiber diameters and size distribution was done using the ImageJ program.

2.4.1 Scanning Electron Microscopy

Scanning Electron Microscopy is an important imaging technique that implements a focused high-energy electron beam to induce electron-sample interactions at the atomic level that then generate a range of readable signals that can reveal information such as crystalline structure, physical orientation, morphology, and chemical composition. Imaging can be performed for samples with areas between 5 microns and 1 cm. (84-87) The focused electron beam is made up of accelerated electrons that contain a high amount of kinetic energy. Upon contact with the sample material, all of this initial kinetic energy is dissipated and resultant signals are recorded as velocity of incident electrons lowers in the solid sample. There are four different types of signals that can be recorded (and four different modes of operation) in SEM; these include backscattered electrons, secondary electrons, x-rays, and cathodoluminescence. (88)

In this study, SEM was done in scanning electron mode. The basic physics of this method is due to the high energy electrons of the incident beam interacting with electrons in the atoms of the sample material. These valence electrons are freed and pass through the bulk of the sample. Secondary electrons can also be produced by interaction with backscattered electrons. Secondary electrons (energies less than 50 eV), are detected by a device consisting of a photomultiplier and light guide coated in aluminum to which a potential electric field is applied that then attracts the released secondary electrons. These attracted electrons then activate an interior layer of phosphor after elevating in energy level and data is collected of energy level and direction. (89)

2.4.2 Energy Dispersive Spectroscopy

Energy dispersive spectroscopy (EDS) was used to analyze the chemical characterization of the materials. An x-ray beam is focused onto the material and results in electron emission from the elements in the material, each corresponding to a unique set of peaks recognizable due to the known atomic structure of certain elements. (90)

2.5 XRD

Crystalline phase analysis was performed using X-Ray Diffraction to investigate phase composition and crystal size for each composition and temperature.

A Panalytical Empyrean Multipurpose X-ray diffractometer with a copper X-ray source (λ=1.54187 Å) was used. Incident beam optics implemented were the Bragg-BretanoHD (BBHD), used to eliminate the Cu K-beta line, with a ¼° divergence slit and a 1° anti-scatter slit. The Pixcel 3D detector was used set to linear array mode. Symmetric scans were performed with a step size of 0.0131 degrees 2θ and a scan range of 10 to 90 degrees 2θ.

2.5.1 X-Ray Diffraction

The concept of X-ray diffraction (XRD) began in the early 20th century when physicists discovered a model to describe the different angles of incidence (θ) that X-ray beams are reflected from crystal faces, known as Bragg's Law. (91)

$$\lambda = 2d_{hkl}sin\theta \quad (3)$$

This law led to a study of diffraction due to many other types of beams with wavelengths close to atomic/molecular distances with the hopes to identify crystal structure of materials

of interest. XRD can accomplish a number of things in terms of material characterization; it can measure size, shape, and stress of small crystal areas, identify unknown material crystalline structure, measure spacing between atomic rows or layers, or determine crystal/atomic orientation.

The general concept is due to X-ray beams interacting with atomic planes in a crystal that then interfere which each other upon leaving. The resultant diffraction pattern is then recorded for analysis.

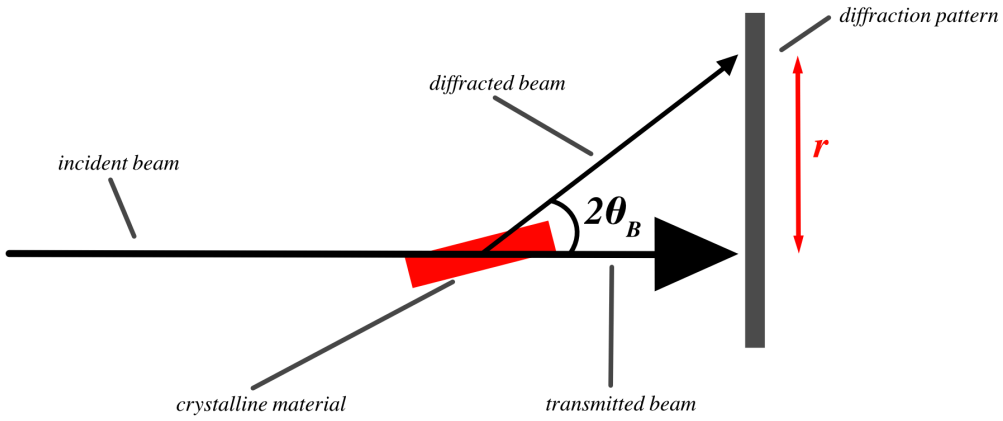

Figure 9. Basic schematic of X-Ray diffraction

2.5.2 Rietvield Refinement

The intensity, height, width, and position of peaks in XRD diffraction patterns are determined by crystal structure of the sample material. The method used in this study to analyze crystal structure of the sample materials was Rietvield refinement, which is a computational fitting method using a nonlinear least squares approach with resulting XRD spectra. (92)

The atomic bond distances in the crystalline sample cause the diffraction peak positions that are seen in an XRD spectrum. To begin, one must consider Bragg's law (2). (93) This calculates the angle θ at which constructive X-ray inference occurs due to scattering from parallel planes of atoms in the material. Bragg's law relies on the wavelength of the incident beam (λ) and the d-spacing for each given unit cell. λ is fixed, but lattice parameters for unit cells of interest must be used to calculate d_{hkl}, the distance between parallel planes of atoms in the crystallographic plane; this unit accounts for peak position changes due to any change due to temperature, pressure, or anything else that would also alter the bond distances in the material. The peak intensities of Bragg peaks is based upon geometrical information about the unit cell of interest and atomic coordination. Bragg peak positions and intensities are described by something known as a peak shape function (PSF), including convolution of dispersion, broadening, background, and sample material functions which mathematically model beam characteristics, sample shape and size, and experimental arrangement. Rietveld, et al, assumed a Gaussian distribution for the convolution of effects and calculated the peak profile at $2\theta_i$ as:

$$y_i = I_k exp\left[\frac{-4\ln(2)}{H_k^2}(2\theta_i - 2\theta_k)^2\right] \quad (4)$$

Here I_k is the intensity of the peak, based on sample material's scattering parameters and reflection multiplicity, H_k is the full-width-half-maximum, and $2\theta_k$ is the position. For each position of interest, it is possible for multiple diffraction peaks to contribute to the data profile, so intensity functions must be integrated over the range of each Bragg peak and peak width and preferred orientation must also be taken into account.

The refinement computational method generally takes the sum of these peak profiles for observed data and "background" calculated data and minimizes a function *M*

which analyzes the difference using a nonlinear iterative least squares fitting method. If W_i is statistical weight function and $y^{ref} = cy^{obs}$, then:

$$M = \sum_i W_i \left\{ y_i^{obs} - \frac{1}{c} y_i^{ref} \right\}^2 \quad (5)$$

In computational software the parameters for calculation are chosen based on crystallographic information, background parameters, symmetry, scale factors, and temperature. (94)

3. RESULTS AND ANALYSIS

3.1 Thermal Analysis

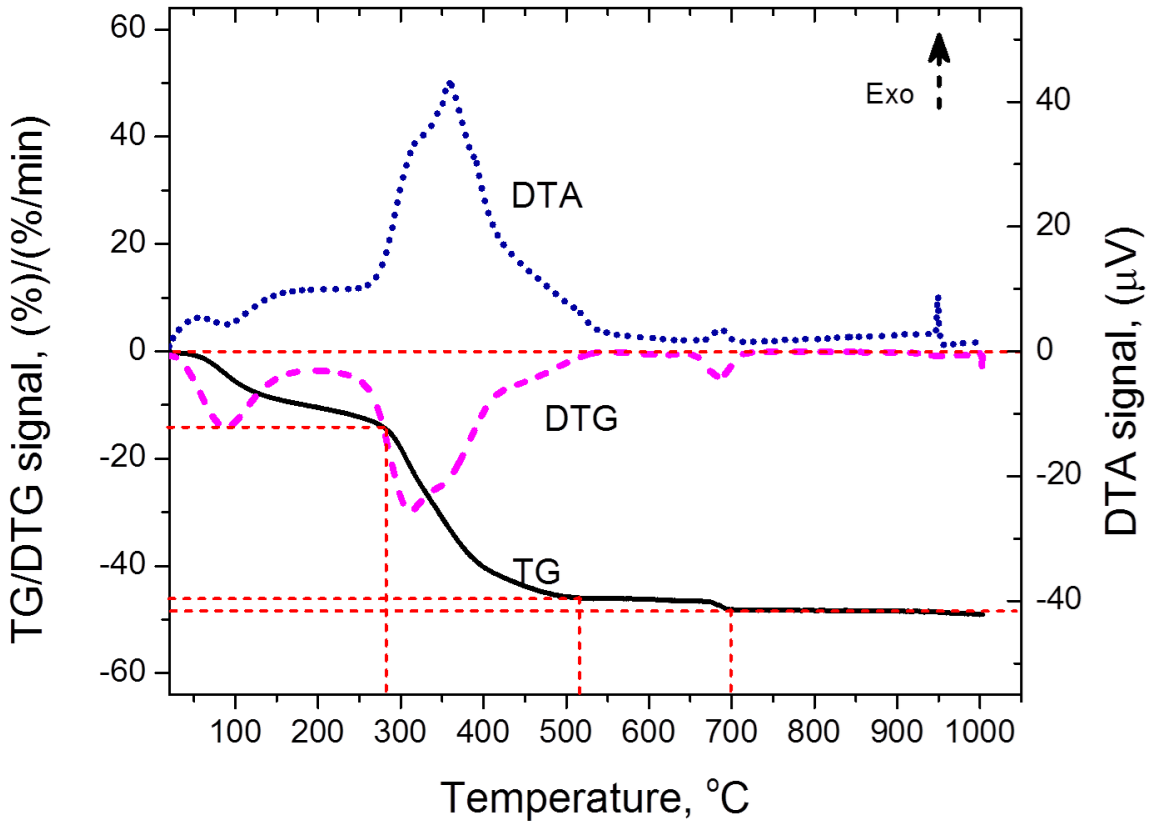

Figure 10. TGA, DTG and DTA data for stoichiometric $ZrTiO_4$ sample

TGA reveals that the material initially has almost no solvent remaining, purely from drying in air and in initial heating on the hotplate. Even starting at 50°C a regular endothermic reaction is not seen; all initial decrease in mass is associated with the removal of acetate groups and hydroxides. Between 50 and 80°C there is about a 20% loss in mass. The mass reduction that is seen between 50 and 280°C is primarily due to hydroxide group loss and substituting acetate groups. There is then a steep drop at around 280°C where almost 50% mass is lost. This can be attributed to loss of residual components, more OH^- groups and then the decomposition of all polymer matrix components through the formation of ions such as CH_2(from vinyl groups), CO_2, HCO_2, N=O, and Carbon ions. This ends around 500°C with some amount of residual carbon and some organics remaining until about 700°C.

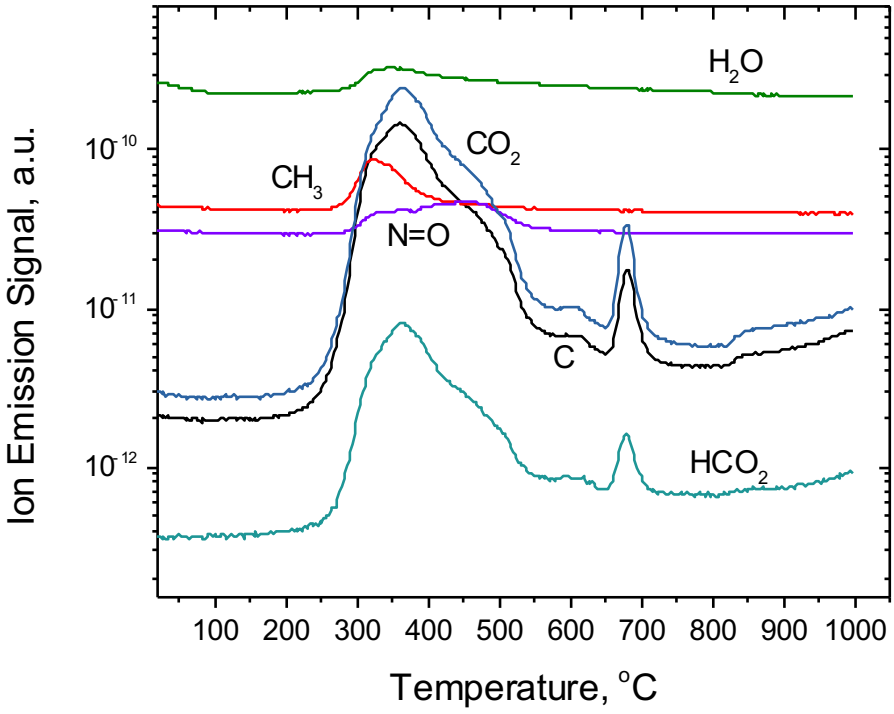

Figure 11. Ion emission signal as a function of temperature for stoichiometric $ZrTiO_4$

There is a clear sharp peak at ~700°C in the DTA curve (Fig. 10) with the corresponding increase in the ion emission signal at that temperature (Fig.11). This small exothermal peak in the DTA curve designates a clear phase transition with formation of crystalline 1:1 Zirconium Titanate. After studying TiO_2 and ZrO_2 ion emission signals for comparison it is clear that they do not have such clear transition peaks. (95-99)

The TGA, DTG, DTA and Ion Emission signal curves helped guide experimental thermal processing regimes. In particular, it was determined that when the fibers were annealed below 700°C, it was important to maintain the low heating rate (less that 5°C/min) to prevent the destruction of fibers. Due to analysis of data, it was clear that the heating procedure could only be accelerated over 700°C without destroying the fibers.

3.2 Precursor and Fiber Flow Characterization

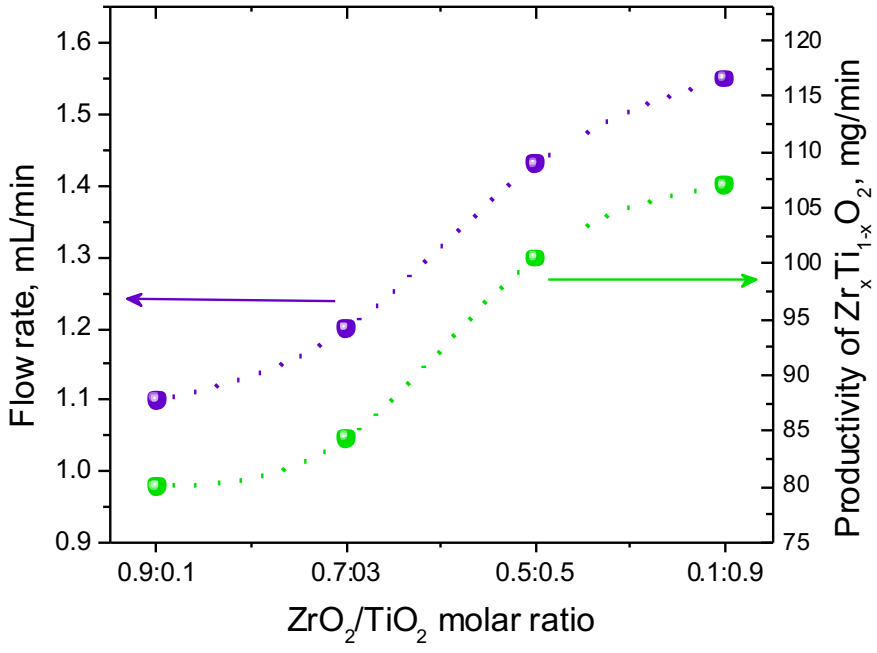

Figure 12. Flow rate and productivity as a function of molar ratio

Flow rate and productivity interestingly increase with increasing the content of titanium alkoxide in the precursor. However, there is only some small decrease in viscosity of the precursor solution with increasing content of titanium alkoxide, while the surface tension of the precursor remains almost constant. Other possible factors that would affect flow rate all change very little with the exception of electrical conductivity. It is perhaps true that in this case the electrical conductivity alone (Fig. 13) drives the changes in the flow rate. Lower conductivity of solution would result in a larger drop in electric field strength across the liquid layer of precursor during the electrospinning process. This could lead to a greater electric field strength in the layer and therefore a greater Coulomb force, the main force in the process of jet formation.

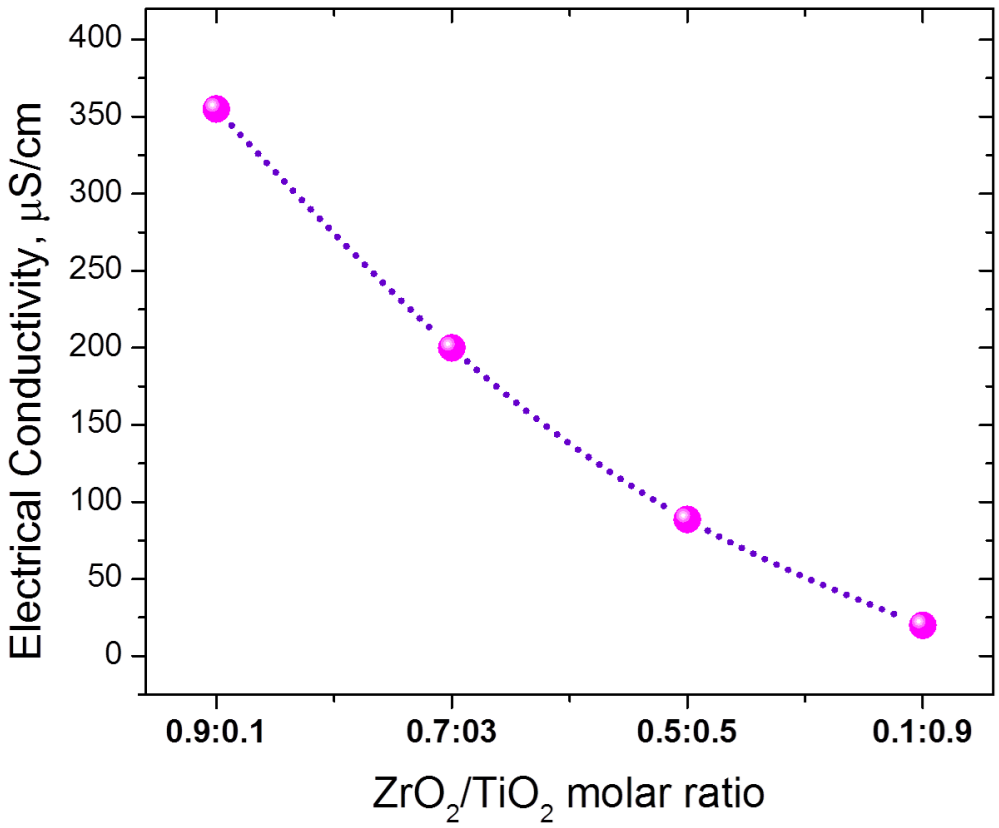

Figure 13. Electrical conductivity of $Zr_xTi_{(2-x)}O_4$ as a function of molar ratio

Clearly, electrical conductivity drops sharply in the precursors with increasing content of titanium alkoxide. This is possibly due to complex reactions due to the chemical nature of both alkoxides and their rates of hydrolysis. With more zirconium alkoxide in the precursor, hydrolysis may occur faster and may cause more water in the resulting solution, which increases ion dissociation and should also increase the conductivity. The mechanism for this phenomenon is not fully yet understood but is of interest for possible future study.

3.3 Fiber Characterization by SEM/EDS

SEM analysis of composite fibers annealed at different temperatures have shown relatively small variations in fiber diameter. (Fig 14) Fiber diameter stays in the average range of about ~250nm to ~360nm for all molar ratios. For each composition, fiber diameter tends to decrease as temperature increases and the smallest fiber diameters are seen for calcination at 1000°C. Interestingly fibers calcined at 1200°C have on average a larger diameter than those at smaller temperatures.

Though variations in size are relatively large, there is a trend with fiber diameter. The size varies very little as a function of the composition of material which can be attributed to the similar viscosity of the precursors or the balance of viscosity and electrical conductivity. Since electrical conductivity increases with more zirconium alkoxide in the precursor, more electric force and therefore thinner fibers should be seen. However, as aforementioned, there is a surprising increase in conductivity for increasing TiO_2, which, if correctly associated with an increase in field strength due to uniform surface tension in the precursors across all compositions, could explain the small variation in diameters due

to opposite effects of field due to both phenomena balancing each other out. Compositions in the middle of the spectrum shrink substantially more than those on either end. This could be attributed to a greater initial microporosity. For calcination at 600°C the range of fiber diameters is between 280 and 340nm. With increased titania content there is only a small increase. As expected, fiber diameter reduces with higher temperatures of calcination and sintering due to densification. Grain size increased noticeably at 1000°C calcination, which is where the smallest fiber diameter is seen. Fibers at this temperature, regardless of grain size and composition, remain intact. Due to gradual grain growth, annealing to 1200°C led to clear axial shrinkage of the fibers and partial sintering of the fibrous structure. The observed increase in fiber diameter, especially pronounced in TiO_2 rich compositions, can thusly be explained.

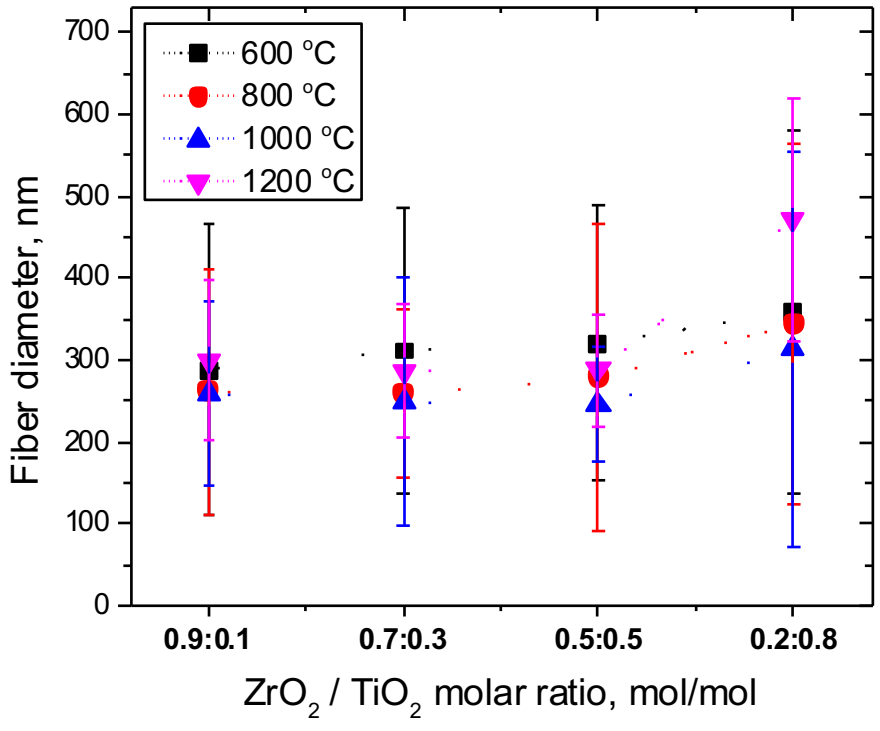

Figure 14. Fiber diameter of $Zr_xTi_{(2-x)}O_2$ as a function of molar ratio

SEM images of $Zr_xTi_{(2-x)}O_4$ samples with different compositions annealed at 600, 800, 1000, and 1200°C are shown in Fig. 15. Figures 15a-15d show all four studied compositions from lowest molar fraction titania (15a) to greatest (15d). Overall the trend across all temperatures is very similar for all compounds. Fiber morphology is smooth and porous at the lower molar fraction titania regime. Fibers begin to show a bit more roughness and possible lack of stability and fragility for the maximum molar fraction titania. The number of apparent surface defects and graininess increases as temperature increases. At 600°C, all fibers are smooth and yet clearly highly porous. At 800°C the internal crystalline structure can be seen more easily due to grain growth. The zirconia rich compounds, however, remain denser and uniform and fibers become grainier. At 1200°C, there are relatively small variations between compositions but the largest grains are observed in titania rich compounds and at stoichiometric composition an interesting surface morphology of individual grains becomes apparent. SEM images reveal a clear stability of fibers even up to 1200°C calcination, as fibers clearly remain intact with very little noticeable fusion between fiber.

Fig. 16 shows the stoichiometric compound annealed to 600°C. It is very smooth and clearly very porous. At 800°C (fig. 17) a millet-like surface topology begins to form and the porosity becomes clearer. At 1000 and 1200°C, grain size grows significantly but the fibers still appear to be completely stable.

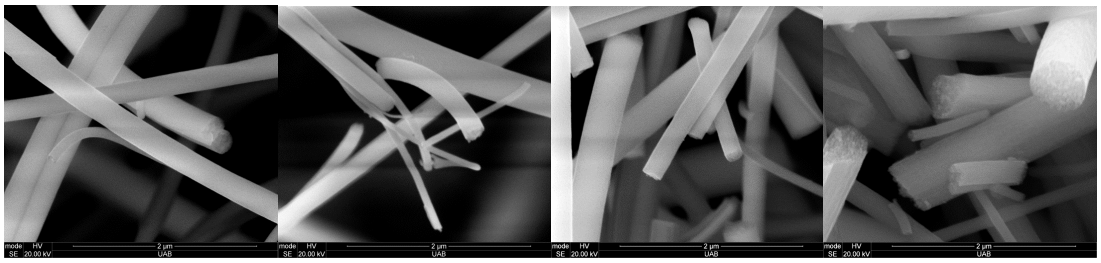

a) b) c) d)

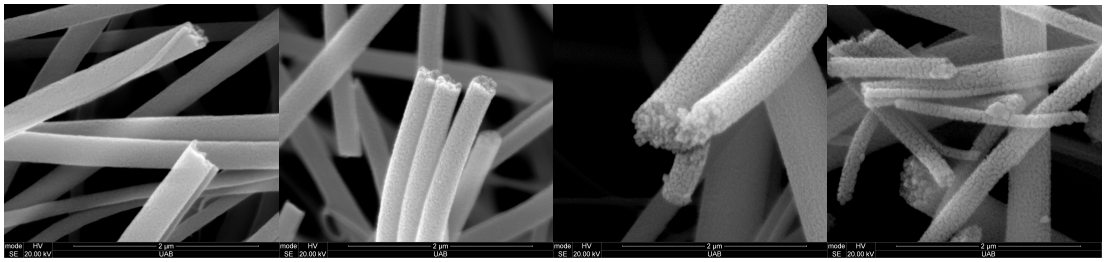

e) f) g) h)

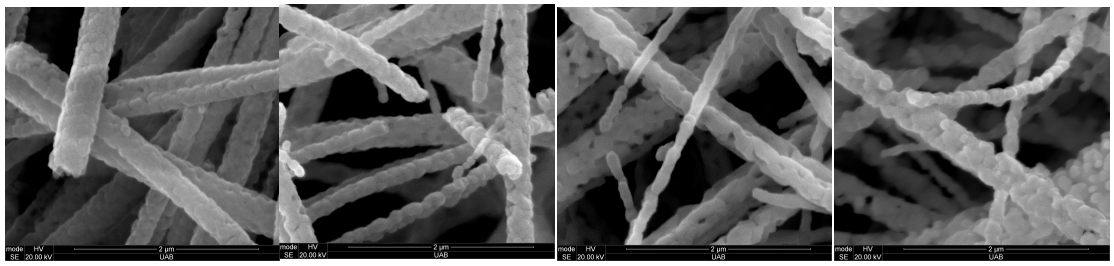

i) j) k) l)

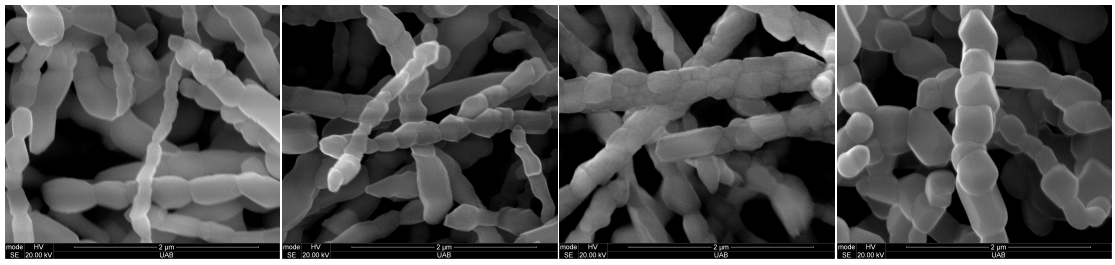

m) n) m) o)

Figure 15. SEM images at a scale of $2\mu m$ for all compositions and temperatures of interest. a)-d) are TiO_2:ZrO_2 compositions of 0.9:0.1, 0.7:0.3, 0.5:0.5 and 0.2:0.8 at 600°C. e)-f) are at 800°C. i)-l) are at 1000°C. m)-o) are at 1200°C.

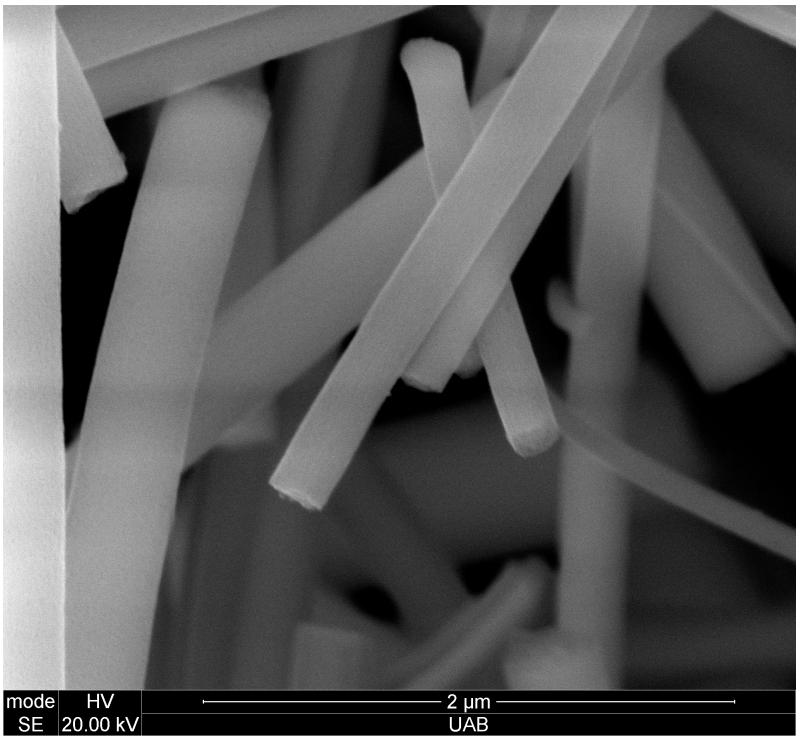

Figure 16. SEM image at $2\mu m$ magnification of 0.5:0.5 molar ratio ZrO_2:TiO_2 at 600°C

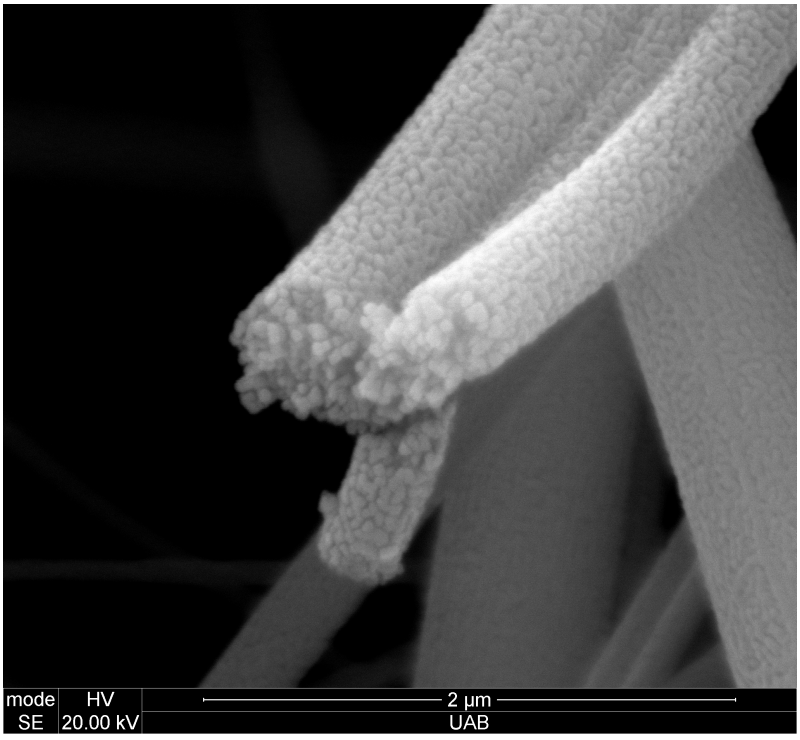

Figure 17. SEM image at $2\mu m$ magnification of 0.5:0.5 molar ratio ZrO_2:TiO_2 at 800°C

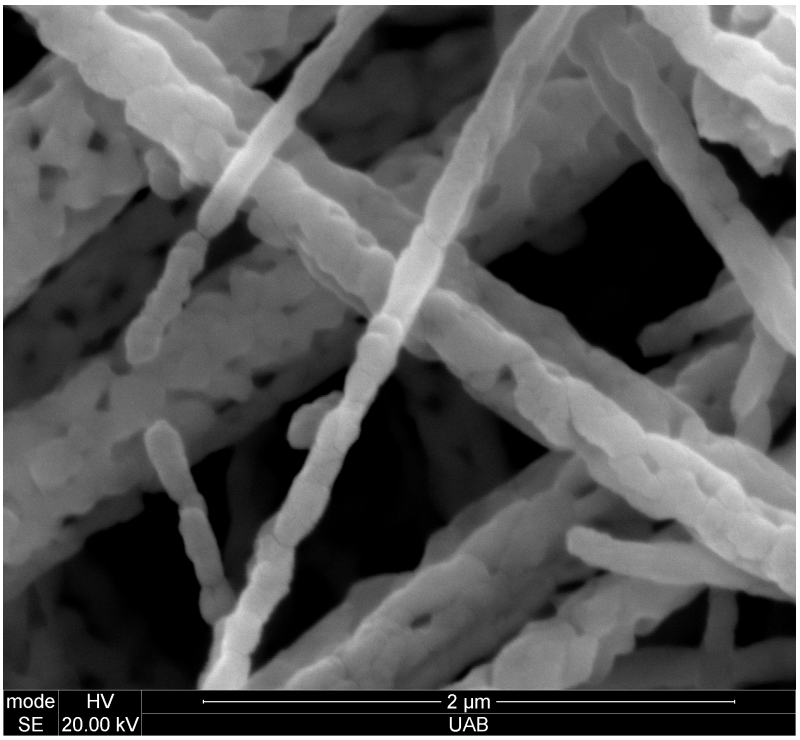

Figure 18. SEM image at $2\mu m$ magnification of 0.5:0.5 molar ratio ZrO_2:TiO_2 at 1000°C

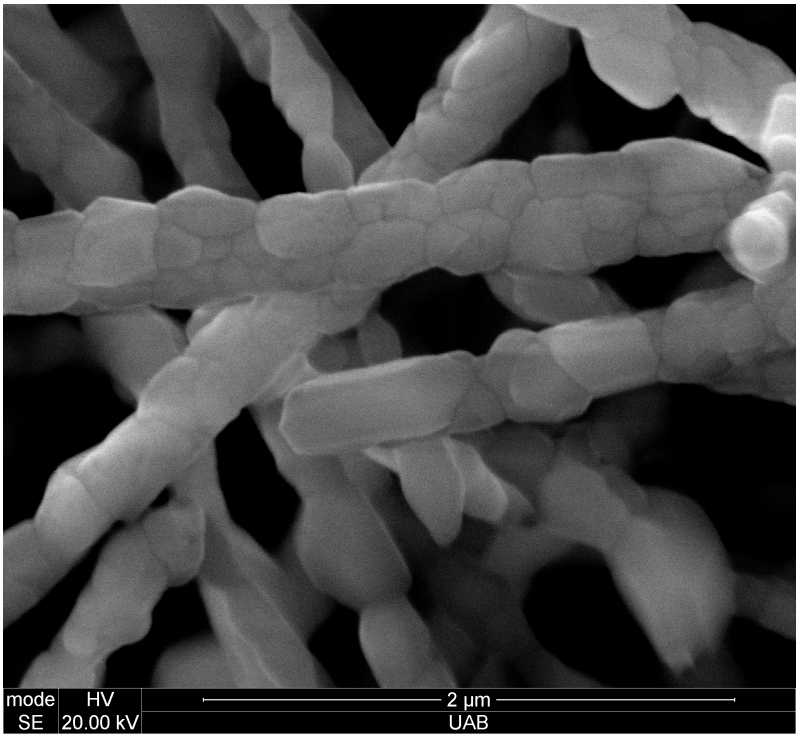

Figure 19. SEM image at $2\mu m$ magnification of 0.5:0.5 molar ratio ZrO_2:TiO_2 at 1200°C

It is clear from EDS data for the targeted molar ratios (fig. 20-23) that the precursor preparation, electrospinning, and annealing procedures were highly successful in achieving desired compositions. For the desired 1:1 molar ratio, there was only a 0.83mol% deviation from pure stoichiometry with a resultant molar ratio of 1.02:0.98. For the targeted 9:1 molar ratio composition exists a 2.67 mol% error with a result of 8.8:1.2 molar ratio. This is slightly more significant but the composition is still of interest. For the targeted 7:3 molar ratio there is a .7 mol% error corresponding to a ratio of 7.07:2.93, which is similar to the results from the 1:1 ratio, with negligible deviation from desired composition. Finally, for the targeted 2:8 molar ratio exists a percent error of 1.1 mol% corresponding to an achieved molar ratio of 1.89:8.11. This is slightly more significant than percent error for 1:1 and 7:3 targeted ratios but is still well within negligible means. The observed variations in the material composition are explained only by the precision of mixing of rather small quantities of the precursor components which led to the magnitudes of the errors. The EDS data shows that this mixed sol gel and electrospinning method could be a great, consistent, and reasonably accurate method to obtain materials of desired molar compositions in industrial or larger scale production.

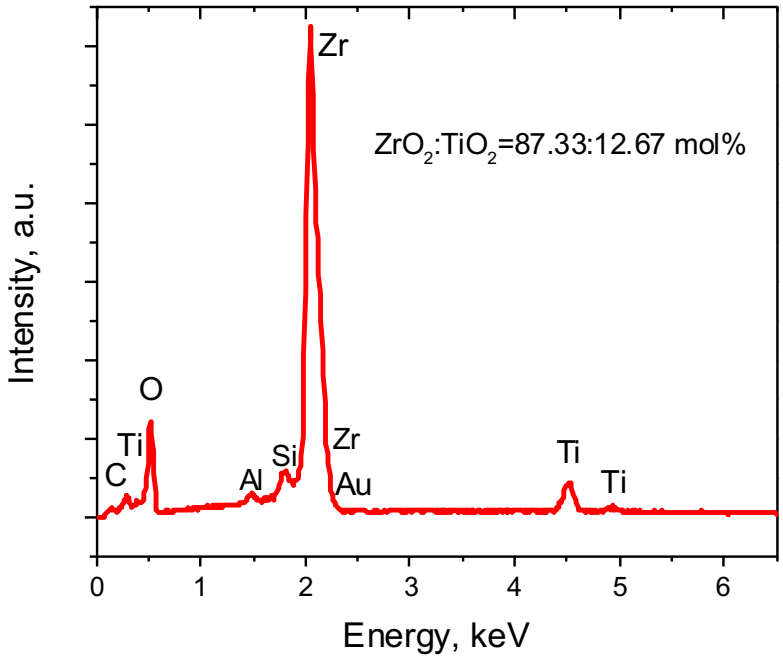

Figure 20. EDS data for targeted 9:1 ZrO_2:TiO_2 ratio

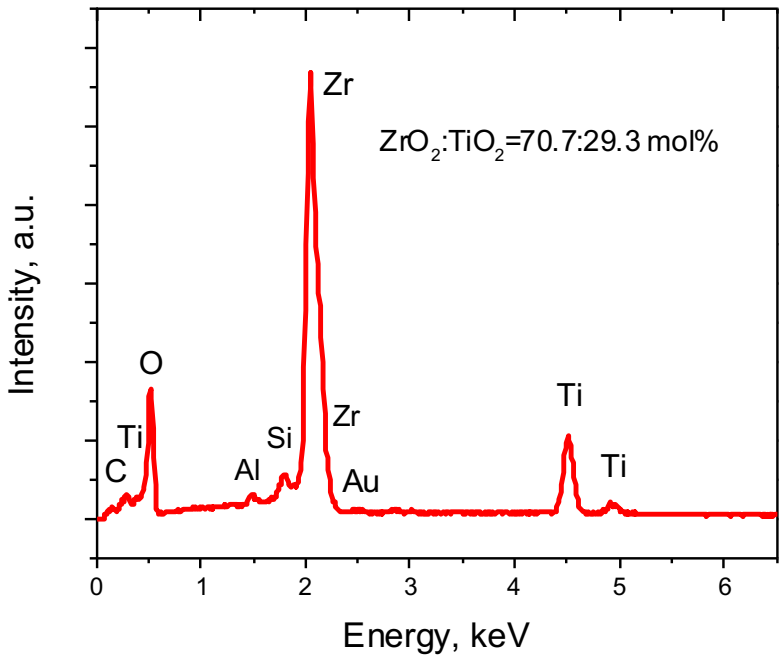

Figure 21. EDS data for targeted 7:3 ZrO_2:TiO_2 ratio

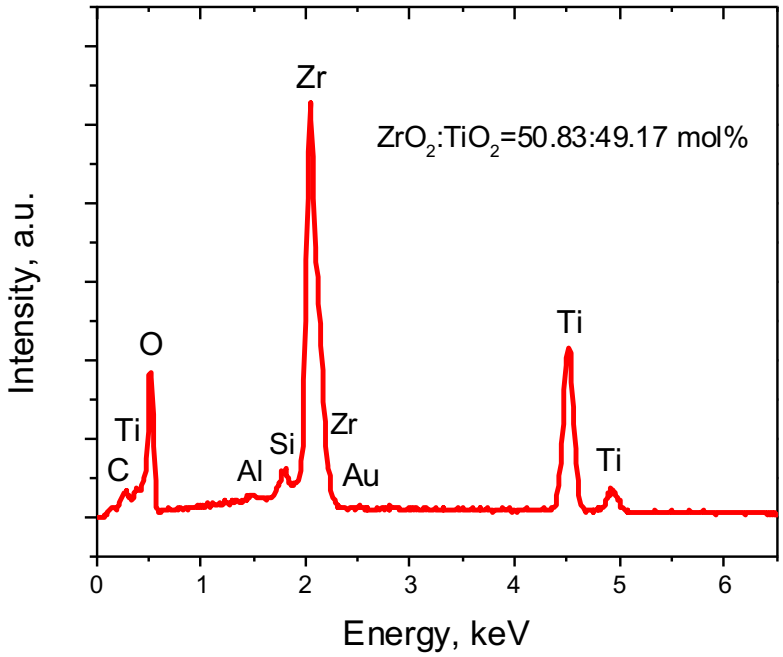

Figure 22. EDS data for targeted 1:1 ZrO_2:TiO_2 ratio

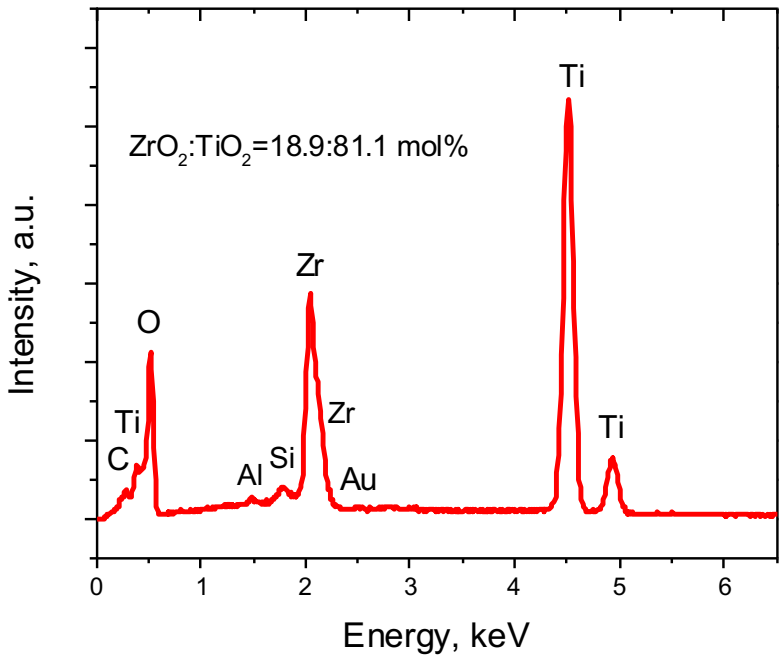

Figure 23. EDS data for targeted 2:8 ZrO_2:TiO_2 ratio

3.4 Crystallization and Phase Analysis

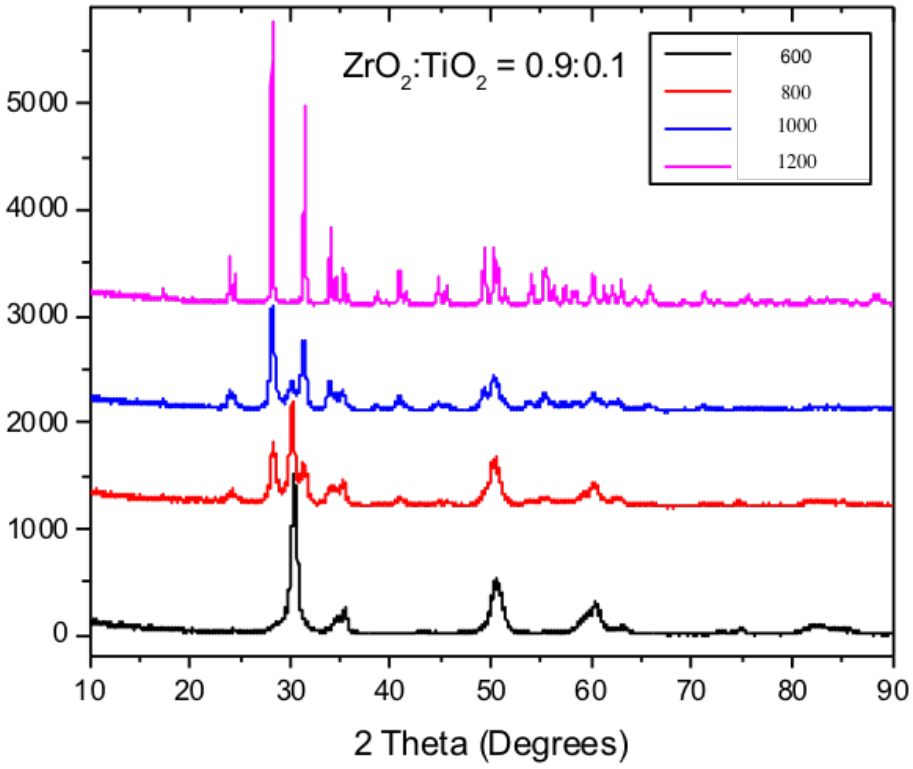

Figure 24. XRD Spectra for targeted molar ratio ZrO_2:TiO_2 = 0.9:0.1

According to XRD data for the targeted ratio of ZrO_2:TiO_2 = 0.9:0.1 (Fig. 24), the material calcined at 600°C is in the form of a solid solution of Titania in tetragonal crystalline Zirconia with a minor monoclinic phase and tetragonal ZrO_2 phase mean crystallite size of 13.5 nm. At 800°C co-exists 17.1nm tetragonal ZrO_2 and 13.7nm monoclinic ZrO_2. At 1000°C there are stable 19.8 nm tetragonal ZrO_2 and 18nm monoclinic ZrO_2. Sintering at 1200 °C finally brings full conversion to monoclinic ZrO_2 with a 47.9nm crystallite size. The initial formation of metastable tetragonal phase is associated with the spontaneous nucleation of very small zirconia crystallites with high

surface energy which is favorable for the formation of tetragonal phase. This phase is stabilized by the small size of crystallites, presence of oxygen vacancies, and carbon residue from the decomposing polymer matrix. (102) As temperature increases in the present study, development of monoclinic phase is certainly seen, but tetragonal phase is still clearly present, particularly due to the still small size of crystallites (less than 30 nm). Grain size increases for tetragonal phase and at higher temperatures there is an energy (kinetic) associated process forming more favorable conditions for monoclinic nucleation. Even at 1200°C there is no trace of formation of a separate unmixed Titania phase. It is possible that Titania moderately stabilizes the tetragonal phase at this mol% as the transition is slightly slower than in pure Zirconia.

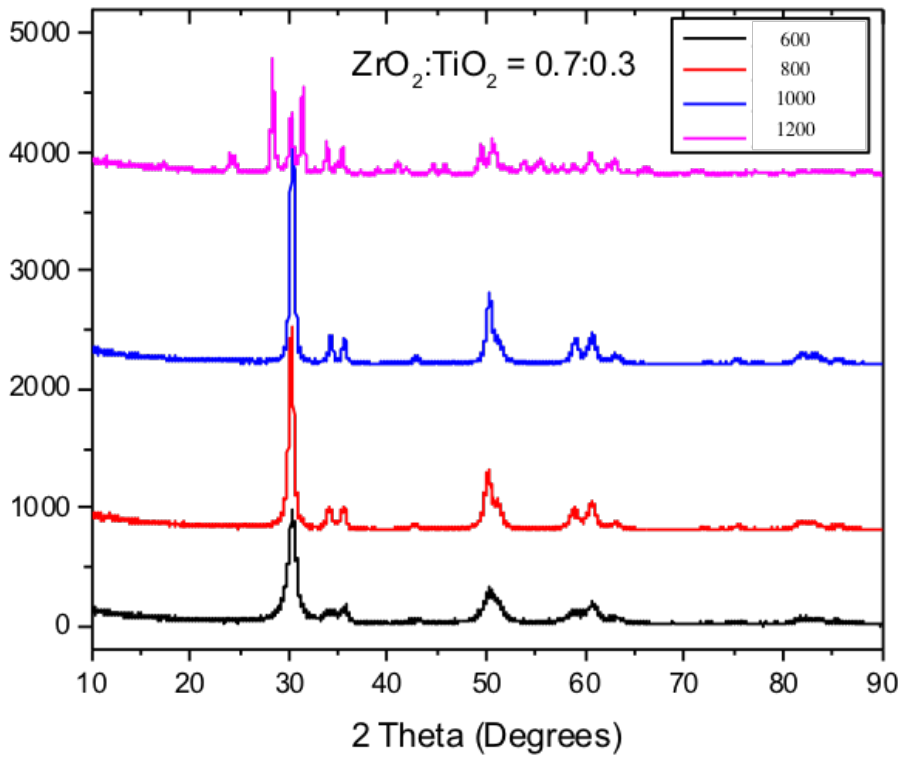

Figure 25. XRD Spectra for targeted molar ratio ZrO_2:TiO_2 = 0.7:0.3

$Zr_xTi_{(2-x)}O_4$ Nanofibers with 0.7:0.3 targeted molar ratio (x=1.0) have an initial stable doped tetragonal phase with no trace of monoclinic (Fig 25). Crystal sizes for tetragonal phase, stable up to 1000°C, are 17.8nm at 1000°C, 14.7nm at 800°C and 9.1nm at 600°C. At 1200°C there is a mixture of tetragonal and monoclinic ZrO_2 with crystal sizes of 21.7nm (tetragonal) and 27.3nm (monoclinic). For TiO_2-ZrO_2 composites prepared from coarse-grained powder with such molar ratio, only a 13-16% solubility of TiO_2 in tetragonal ZrO_2 has been reported in literature, which is certainly much smaller than the apparent ~30+% solubility seen in the study of this AFES produced material. (100) EDS confirmed that close to the amount of desired Titania does indeed exist in the samples, but no separate phase is seen, just a solid solution. Tetragonal phase is clearly stable until 1000°C, and it is still present after sintering at 1200°C. Similar solubility levels have been reported only in a high pressure study. (101) In the present study, no new phases are seen, but it is possible that the conditions provided in this study allow for the same kind of stabilizing factor as in high pressure studies. Sol gel transformation is explained by two factors: grain size and chemical composition. For Zirconia, it has been seen that, due to Gibb's surface energy levels, crystalline sizes less than ~30nm are metastable, and unless they exceed that dimension, no monoclinic phase forms. (95) The chemical composition of the precursors is also very important. In coarse-grained powder mixing, researchers are mixing pure oxides. In sol gel, there exist OH^- groups, carbon, impurities, and therefore many oxygen vacancies. Due to these factors, there seems to be more interatomic mixing as Titania is added when stabilized. The small crystalline size and presence of oxygen vacancies and defects on an initial chemical level could provide enough surface energy and associated hydrodynamic stress (in this case an analog for pressure in the high-pressure

studies) to provide conditions for more TiO_2 dissolved in ZrO_2. These conditions stabilize the system much in the same way as in imposed high pressure conditions. It is a self-compressed and high energy system. Both high pressure and high stress conditions limit the flow of defects upon mixing.

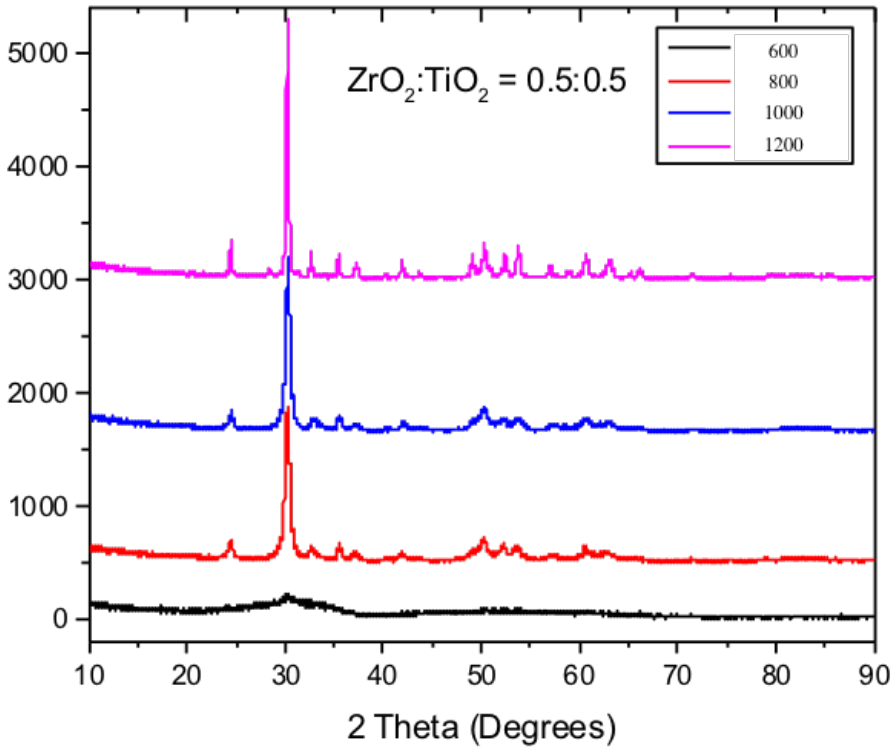

Figure 26. XRD spectra for targeted molar ratio ZrO_2:TiO_2=0.5:0.5

$ZrxTi_{(2-x)}O_4$ Nanofibers with 1:1 targeted molar ratio (x=1.0) show XRD spectra at 600°C and 800°C corresponding to a practically single $ZrTiO_4$ phase with a crystallite size of ~17.5 nm (Fig. 26). There is potentially a small amount of TiO_2 stabilized t-ZrO_2, accounting for minor peak shift at ~30° 2θ and minor peak enhancement at ~51° 2θ. This is mainly only noticeable with data from fibers annealed to 1200°C. At 600°C a practically

amorphous structure is seen. There is only perhaps a tetragonal Zirconia peak due to a little non-stoichiometry (some excess of ZrO_2) of the material and the favorable conditions for crystallization of this phase at 600°C. Around 700°C the material quickly crystallizes (as confirmed by EDS) and the XRD pattern for 800°C calcined sample shows that the amorphous fraction is converted to a single phase $ZrTiO_4$ stoichiometric compound. Excess monoclinic ZrO_2 is clearly seen as a separate peak at 1200°C. As mentioned, a very small amount of monoclinic ZrO_2 mixture appears at 1200°C with crystal sizes of tetragonal phase ranging from 12.2nm-15.3nm-17.1nm-33.3nm for 600, 800, 1000, 1200°C, and monoclinic ZrO_2 at 23.1nm.

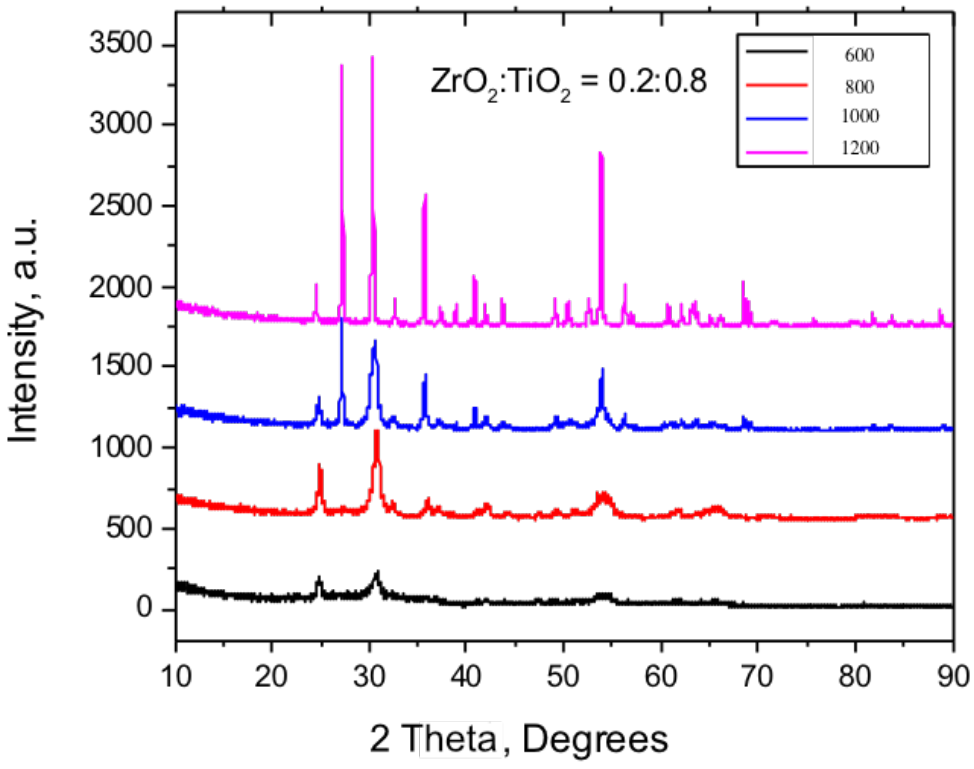

Figure 27. XRD Spectra for targeted molar ratio ZrO_2:TiO_2 = 0.2:0.8

In XRD patterns for the sample for targeted molar ratio ZrO_2:TiO_2 = 0.2:0.8 (Fig. 27), it is observed that even at 600°C, crystallization of two phases occur. At 30°2θ the stoichiometric compound is seen and at 25°2θ a peak appears that corresponds to anatase. Zirconium oxide is most probably still fully dissolved and simply forming a solid solution. Rutile appears at 800°C and its content increases to where anatase begins to breakdown as rutile forms. Between 25 and 30°2θ rutile is seen with a larger grain size. At 1200°C there is no remaining anatase, only rutile phase. From the powder diffraction database and Rietvield analysis, that phase was identified as $Zr_{0.33}Ti_{0.67}O_2$ which is represented by mean crystallite size 14nm at 600°C, 13.2nm at 800°C and 11nm at 1000°C. Then exists some anatase, 20.1nm at 600°C and 21.8nm at 800°C. Rutile forms at 800°C and finally $Zr_{0.45}Ti_{0.55}O_2$ (basically $ZrTiO_4$) forms at 1200°C with a 48.1nm size and rutile with a 62.3nm crystal size.

3.4.1 Summary

After looking at four different compositions of ZrO_2-TiO_2 at four different temperatures within the low temperature regime, this study finds 16 difference reference points which can be compared with the results of the classic phase diagram. (Fig 28)

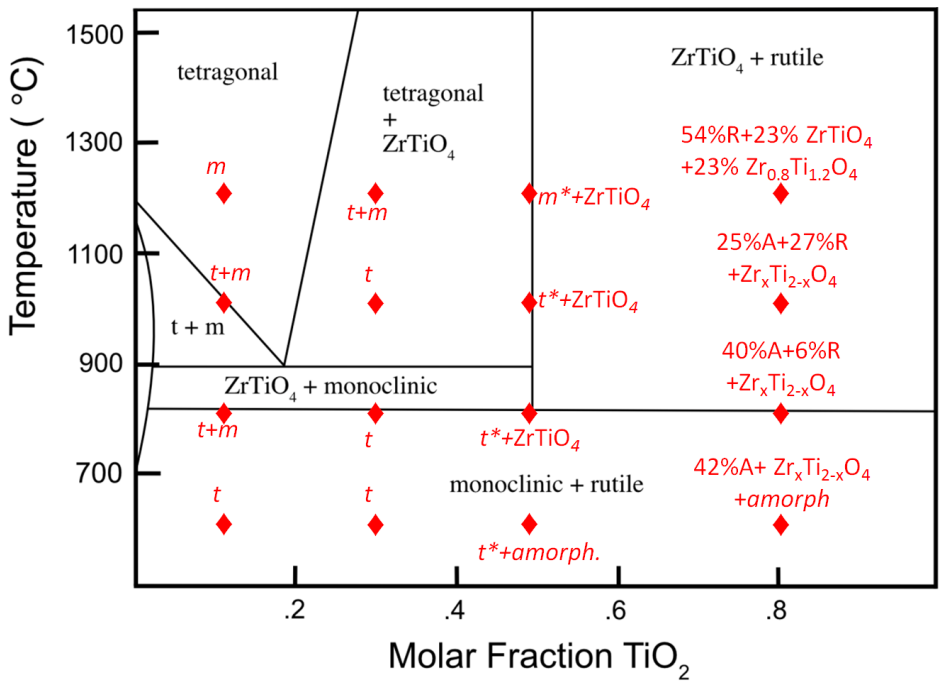

Figure 28. Classical phase diagram with current study results

For the molar ratio of ZrO_2/TiO_2 of 0.9:0.1, the results of this study show an initial single phase of tetragonal ZrO_2 after calcination at 600°C that gradually converts to monoclinic phase ZrO_2 after calcination at higher temperatures. It is possible that it follows the general mechanism of traditional zirconia phase transformation, i.e. where it converts to tetragonal ZrO_2 above 1100°C and becomes fully monoclinic after sintering at 1200°C and then cooling to room temperature.

For the molar ratio of ZrO_2/TiO_2 of 0.7:0.3, the results of this study show an initial single phase of tetragonal ZrO_2 after calcination at 600°C that is stable up to at least 1000°C. After sintering at 1200°C and then cooling to room temperature it only partially converts to monoclinic phase. No precipitation of TiO_2 phases was observed. It seems that the material represents a substitutional solid solution of TiO_2 in ZrO_2.

For the molar ratio of ZrO_2/TiO_2 of 0.5:0.5, the results of this study show that, due to a minor non-stoichiometry, the excess zirconia crystallizes as tetragonal phase while the rest of the material remains amorphous after calcination at 600°C. Around 700°C, zirconium titanate ($ZrTiO_4$) phase crystallizes according to TGA data. This is then the main phase in materials calcined at 800°C. A tegragonal ZrO_2 impurity phase is stable until at least 1000°C where it then converts to monoclinic ZrO_2 after sintering at 1200°C. During this transition, $ZrTiO_4$ phase remains stable and nanocrystalline.

For the molar ratio of ZrO_2/TiO_2 of 0.2:0.8, the results of this study show that it is composed of the anatase phase of TiO_2 and non-stoichiometric nanocrystalline $Zr_xTi_{2-x}O_4$ (may be a mixture of several zirconium titanates) with some amorphous phase after calcination at 600°C. Rutile phase appears after calcination at 800°C and then the system gradually converts into a distinct mixture of rutile (54 mol%) and two zirconia titanate nanocrystalline phases (one stoichiometric and another with excess TiO_2) after sintering at 1200°C.

4 CONCLUSIONS

This study successfully developed and explored a process for high throughput production of titania and zirconia based fibers in a large range of compositions. It was clearly demonstrated that $Zr_xTi_{(2-x)}O_4$ nanofibrous materials with various molar ratios of zirconia and titania can be effectively fabricated by a high yield, free surface AC electrospinning technique from precursors based on metal alkoxides.

A novel, high-yield free surface alternating field electrospinning (AFES) process was used to efficiently produce desired fibrous materials from optimized precursor

solutions based on titanium and zirconium alkoxides and the polymer polyvinylpyrrolidone (PVP).

Productivity of the AFES process was clearly affected by the molar ratio of titanium and zirconium alkoxides in precursor solution. Increase in oxide yield from 4.8 to 6.4 g/h was seem when ZrO_2/TiO_2 molar ratio changed from 0.9/0.1 to 0.2/0.8.

Optimal thermal processing was performed at a slow rate of heating up to 700°C due to EDS data. Processing of the materials in air between 600 and 1200°C resulted in ceramic nanofibers with fiber diameters ranging from 100 to 600nm, with averages varying between 250 and 420nm, depending on composition and temperature.

Chemical composition of the fabricated $Zr_xTi_{(2-x)}O_4$ nanofibrous materials had only a moderate effect on textural properties of the fibers, but was critical to determining phase composition after thermal processing.

The formation of nanocrystalline zirconia fibers composed of single phase tetragonal ZrO_2 (t-ZrO_2) was observed at up to 28 mol% of TiO_2. The t-ZrO_2 phase was stable up to 1000 °C when the content of TiO_2 was 28 mol%. This concentration of TiO_2 exceeds the dissolution limit of titania reported in literature. Nevertheless, there was no precipitation of TiO_2 observed when the material was sintered at 1200 °C and partially converted to monoclinic ZrO_2. The small crystalline size and chemistry of sol gel precursor mixing of the material produced in this study could provide enough surface energy and associated hydrodynamic stress to provide conditions for more TiO_2 in ZrO_2.

Single phase $ZrTiO_4$ nanofibers were formed from the ZrO_2/TiO_2 precursors with 1.0/1.0 molar ratio. This zirconium titanate phase started to crystallize at 600 °C and was stable during sintering at 1200 °C for two hours. During this time, it remained a

nanocrystalline material with the average crystallite size of 33±3 nm. There was a small amount of monoclinic zirconia seen to develop in this sample which can be associated with some non-stoichiometry of achieved material.

It has been suggested that the initially formed crystalline phases, their stability and transformations are determined by the atomic scale interaction of the precursor components, presence of carbonaceous residue during the decomposition of polymer components, surface energy and defect states (in particular oxygen vacancies) of initially formed crystallites with the dimensions less than 30 nm.

4. REFERENCES

1. Ahmed S. Yasin, M. Obaid, Mohamed H. El-Newehy, Salem S. Al-Deyab, Nasser A.M. Barakat, Influence of $TixZr_{(1-x)}O_2$ nanofibers composition on the photocatalytic activity toward organic pollutants degradation and water splitting, Ceramics International, Volume 41, Issue 9, Part B, 2015, Pages 11876-11885

2. N.A.M. Barakat, A.Taha, M.Motlak, M.M.Nassar, M.S.Mahmoud, S.S. Al-Deyab, M.El-Newehy, H.Y.Kim, ZnO and Fe_2O_3–incorporated TiO_2 nanofibers as super effective photocatalysts for watersplitting under visible light radiation, Appl.Catal.A: Gen.481(0)(2014) 19–26.

3. G. Carotenuto, Y.-S.Her, E.Matijevic, Preparation and characterization of nanocomposite thin films for optical devices, Ind. Eng. Chem. Res. 35 (9) (1996)2929–2932.

4. S.U. Khan, M. Al-Shahry, W.B. Ingler, Efficient photochemical water splitting by a chemically modified n-TiO_2, Science297(5590)(2002) 2243–2245.

5. N.A. Barakat, M.A. Kanjawal, I.S. Chronakis, H.Y. Kim, Influence of temperature on the photodegradation process using Ag-dopedTiO_2 nanostructures: negative impact with the nanofibers, J.Mol.Cat.A:Chem. 336(1)(2012)333–340.

6. S. Šegota, L. Ćurković, D.Ljubas, V.Svetličić, I.F.Houra, N.Tomašić, Synthesis, characterization and photocatalytic properties of sol–gel TiO_2 films, Ceram.Int.37 (4)(2011) 1153–1160.

7. G. Wang, H.Wang, Y.Ling, Y.Tang, X.Yang, R.C. Fitzmorris, C. Wang, J.Z.Zhang, Y.Li, Hydrogen-treated TiO_2 nanowire arrays for photo-electrochemical watersplitting, NanoLett.11(7)(2011)3026–3033.

8. T. R. Li, Y. W. Li, Z. Y. Bai, X. C. Peng, Z. Q. Zhong and T. He, Appl. Mech. Mater., 2013, 295-298, 2227.

9. Y. Wang, Y. He, Q. Lai and M. Fan, J. Environ. Sci.-China, 2014, 26, 2139.

10. D. P. MacWan, P. N. Dave and S. Chaturvedi, J. Mater. Sci., 2011, 46, 3669.

11. T. D. Malevu, B. S. Mwankemwa, S. V. Motloung, K. G. Tshabalala and R. O. Ocaya, Physica E, 2019, 106, 127.

12. J. H. Lee, J. W. Kim, J. M. Kim and S. J. Choung, Appl. Chem. Eng., 2013, 24, 231.

13. X. P. Wu, Key Eng. Mater., 2017, 727, 314.

14. A. J. Gardecka, C. Bishop, D. Lee, S. Corby, I. P. Parkin, A. Kafizas and S. Krumdieck, Appl. Catal., B, 2018, 224, 904.

15. J. Zhang, B. Wu, L. Huang, P. Liu, X. Wang, Z. Lu, G. Xu, E. Zhang, H. Wang, Z. Kong, J. Xi and Z. Ji, J. Alloys Compd., 2016, 661, 441.

16. M. Ghadiry, M. Gholami, L. C. Kong, C. W. Yi, H. Ahmad and Y. Alias, Sensors (Switzerland), 2015, 16, 39.

17. D. Wu, S. Zhang, S. Jiang, J. He and K. Jiang, J. Alloys Compd., 2015, 624, 94.

18. S. Gatla, N. Madaan, J. Radnik, V. N. Kalevaru, M. M. Pohl, B. Lücke, A. Martin, U. Bentrup and A. Brückner, J. Catal., 2013, 297, 256.

19. C. A. Walenta, S. L. Kollmannsberger, C. Courtois, R. N. Pereira, M. Stutzmann, M. Tschurl and U. Heiz, Phys. Chem. Chem. Phys., 2019, 21, 1491.

20. Z. Liu, V. Sriram and J. Y. Lee, Appl. Catal. B, 2017, 207, 143.

21. J. C. Bear, V. Gomez, N. S. Kefallinos, J. D. McGettrick, A. R. Barron and C. W. Dunnill, J. Colloid Interface Sci., 2015, 460, 29.

22. A. Kim, D. P. Debecker, F. Devred, V. Dubois, C. Sanchez and C. Sassoye, Appl. Catal. B, 2018, 220, 615.

23. J. Li, H. Qiao, Y. Du, C. Chen, X. Li, J. Cui, D. Kumar and Q. Wei, Sci. World J., 2012, 2012, 154939.

24. C. Ligon, K. Latimer, Z. D. Hood, K. D. Gilroy, and K. Senevirathne, RSC Adv., 2018, 8, 32865.

25. Xuesong Zhao, Guan Zhang, Zhenghua Zhang, TiO2-based catalysts for photocatalytic reduction of aqueous oxyanions: State-of-the-art and future prospects, Environment International, Volume 136, 2020, 105453, ISSN 0160-4120

26. Green, D. J.; Hannink, R.; Swain, M. V. (1989). Transformation Toughening of Ceramics. Boca Raton: CRC Press. ISBN 0-8493-6594-5.

27. Heuer, A.H.; Hobbs, L.W., eds. (1981). Science and Technology of Zirconia. Advances in Ceramics. 3. Columbus, OH: American Ceramic Society. p. 475.

28. Claussen, N.; Rühle, M.; Heuer, A.H., eds. (1984). Proc. 2nd Int'l Conf. on Science and Technology of Zirconia. Advances in Ceramics. 11. Columbus, OH: American Ceramic Society.

29. Tsai, M.C., Lin, G.T., Chiu, H.T. et al. Synthesis of zirconium dioxide nanotubes, nanowires, and nanocables by concentration dependent solution deposition. J Nanopart Res 10, 863–869

30. Bao J, Xu D, Zhou Q, Xu Z (2002) An array of concentric composite nanostructure of metal nanowires encapsulated in zirconia nanotubes: preparation, characterization, and magnetic properties. Chem Mater 14:4709–4713

31. Polliotto, V., Albanese, E., Livraghi, S., Indyka, P., Sojka, Z., Pacchioni, G., Giamello, E. Fifty-Fifty Zr-Ti Solid Solution with a TiO2-Type Structure: Electronic Structure and Photochemical Properties of Zirconium Titanate $ZrTiO_4$ (2017) Journal of Physical Chemistry C, 121 (10), pp. 5487-5497.

32. A.E. McHale and R.S. Roth, Investigation of the Phase-Transition in ZrTiO4 and ZrTiO4-SnO2 Solid-Solutions, Journal of the American Ceramic Society 66 (1983) C18-C20.

33. A.E. McHale and R.S. Roth, Low-Temperature Phase-Relationships in the System ZrO2-TiO2, Journal of the American Ceramic Society 69 (1986) 827-832.

34. Holbig, Eva. (2008). The Effect of Zr-Doping and Crystallite Size on the Mechanical Properties of TiO2 Rutile and Anatase.

35. Simonenko, E.P., Simonenko, N.P., Kopitsa, G.P., Mokrushin, A.S., Khamova, T.V., Sizova, S.V., Khaddazh, M., Tsvigun, N.V., Pipich, V., Gorshkova, Y.E., Sevastyanov, V.G., Kuznetsov, N.T. A sol-gel synthesis and gas-sensing properties of finely dispersed $ZrTiO_4$ (2019) Materials Chemistry and Physics, 225, pp. 347-357.

36. Rouhani, P., Salahinejad, E., Kaul, R., Vashaee, D., Tayebi, L. Nanostructured zirconium titanate fibers prepared by particulate sol-gel and cellulose templating techniques (2013) Journal of Alloys and Compounds, 568, pp. 102-105

37. Hsu, C.-H., Lin, S.-Y., Characterization of ZrTiO4 thin films prepared by sol-gel method (2013) Materials Science in Semiconductor Processing, 16 (5), pp. 1262-1266.

38. Macan, J., Gajović, A., Ivanković, H., Porous zirconium titanate ceramics synthesized by sol-gel process (2009) Journal of the European Ceramic Society, 29 (4), pp. 691-696.

39. U. Troitzsch, TiO2-doped zirconia: Crystal structure, monoclinic-tetragonal phase transition, and the new tetragonal compound Zr3TiO8, Journal of the American Ceramic Society 89 (2006) 3201-3210.

40. U. Troitzsch, A.G. Christy and D.J. Ellis, Synthesis of ordered zirconium titanate $(Zr,Ti)_2O_4$ from the oxides using fluxes, Journal of the American Ceramic Society 87 (2004) 2058-2063.

41. U. Troitzsch, A.G. Christy and D.J. Ellis, The crystal structure of disordered $(Zr,Ti)O_2$ solid solution including srilankite: evolution towards tetragonal ZrO_2 with increasing Zr, Physics and Chemistry of Minerals 32 (2005) 504-514.

42. U. Troitzsch and D.J. Ellis, High-PT study of solid solutions in the system ZrO_2-TiO_2: The stability of srilankite, European Journal of Mineralogy 16 (2004) 577- 584.

43. U. Troitzsch and D.J. Ellis, The ZrO_2-TiO_2 phase diagram, Journal of Materials Science 40 (2005) 4571-4577.

44. M. Daturi, A. Cremona, F. Milella, G. Busca and E. Vogna, Characterisation of zirconia-titania powders prepared by coprecipitation, Journal of the European Ceramic Society 18 (1998) 1079-1087.

45. I.C. Cosentino, E.N.S. Muccillo, R. Muccillo and F.M. Vichi, Low-temperature sol-gel synthesis of single-phase ZrTiO4 nanoparticles, Journal of Sol-Gel Science and Technology 37 (2006) 31-37.

46. A. Bianco, M. Paci and R. Freer, Zirconium titanate: from polymeric precursors to bulk ceramics, Journal of the European Ceramic Society 18 (1998) 1235-1243.

47. E.L. Sham, M.A.G. Aranda, E.M. Farfan-Torres, J.C. Gottifredi, M. Martinez-Lara and S. Bruque, Zirconium titanate from sol-gel synthesis: Thermal decomposition and quantitative phase analysis, Journal of Solid State Chemistry139 (1998) 225-232.

48. Chen, Xiufang & Wang, Xinchen & Fu, Xianzhi. (2009). Hierarchical macro/mesoporous TiO_2/SiO_2 and TiO_2/ZrO_2 nanocomposites for environmental photocatalysis. Energy & Environmental Science - ENERGY ENVIRON SCI. 2. 10.1039/b904012a.

49. Chengxin Fu, Yinyan Gong, Yitao Wu, Jiaqi Liu, Zhen Zhang, Can Li, Lengyuan Niu, Photocatalytic enhancement of TiO2 by B and Zr co-doping and modulation of microstructure, Applied Surface Science, Volume 379, 2016, Pages 83-90, ISSN 0169-4332,

50. Ji Sun Im, Min Il Kim, Young-Seak Lee, Preparation of PAN-based electrospun nanofiber webs containing TiO2 for photocatalytic degradation, Materials Letters, Volume

62, Issues 21–22, 2008, Pages 3652-3655, ISSN 0167-577X, https://doi.org/10.1016/j.matlet.2008.04.019.

51. Su, Chunyan & Tong, Yufeng & Zhang, Mingyi & Zhang, Yue & Shao, Changlu. (2013). TiO2 nanoparticles immobilized on polyacrylonitrile nanofibers mats: A flexible and recyclable photocatalyst for phenol degradation. RSC Adv.. 3. 7503-7512. 10.1039/C3RA40210J.

52. Leyland, Nigel & Carroll (Podporska), Joanna & Browne, John & Hinder, Steven & Quilty, Brid & Pillai, Suresh. (2016). Highly Efficient F, Cu doped TiO2 anti-bacterial visible light active photocatalytic coatings to combat hospital-acquired infections. Scientific Reports. 6. 24770. 10.1038/srep24770.

53. Xue, Hongbo & Jiang, Ya & Yuan, Kechun & Yang, Tingting & Hou, Jianhua & Cao, Chuanbao & Feng, Ke & Wang, Xiaozhi. (2016). Floating photocatalyst of B–N–TiO2/expanded perlite: a sol–gel synthesis with optimized mesoporous and high photocatalytic activity. Scientific Reports. 6. 29902. 10.1038/srep29902.

54. Shahzad, N., Azfar, R.W. Comparison of H2S gas destruction potential using TIO2 nanofibers and nanoparticles. Environ Sci Pollut Res 24, 1133–1136 (2017).

55. Huang, Z.-M., A review on polymer nanofibers by electrospinning and. Composites Science and Technology 63, 2223–2253 (2003).

56. C. J. Luo, S. D. S. E. S. E. P. a. M. E., Electrospinning versus fibre production methods: from specifics to technological convergence. Chem Soc Rev 41, 4708-4735 (2012).

57. Y.Dai, W. L. F. S. X., Ceramic nanofibers fabricated by electrospinning and and their application in catalysis, environmental science, and energy technology. Polym. Adv. Technol. 22, 326-338 (2001).47

58. D. Malwal, P. G., Fabrication and applications of ceramic nanofibers in water remediation: A review. Crit. Rev. Environ. Sci. Technol. 46, 500-534 (2016).

59. Collins, G., Federici, J., Imura, Y., and Catalani, L.H. (2012) Charge generation, charge transport, and 246. residual charge in the electrospinning of polymers: a review of issues and complications. J. Appl. Phys., 111, 044701–044718.

60. Jiajia Xue, Tong Wu, Yunqian Dai, and Younan Xia. Chemical Reviews 2019 119 (8), 5298-5415

61. P. Pokorny, E. Koštáková, F. Sanetmik,P. Mikes, J. Chvojka, T. Kalous, M. Bilek, K. Pejchar, J. Valtera, D. Lukaš, Effective AC needleless and collectorless electrospinning for yarn production, Phys. Chem. Chem. Phys.16 (2014) 26816–26822.

62. S. Sarkar, S. D. G. T., Biased AC electrospinning of aligned polymer nanofibers.

Macromolecular Rapid Comm. 28, 1034-1039 (2007).

63. Song, J., Wang, X., Yan, J. et al. Soft Zr-doped TiO_2 Nanofibrous Membranes with Enhanced Photocatalytic Activity for Water Purification. Sci Rep 7, 1636 (2017).

64. Noguchi, T. and Mizuno, M., Phase changes in solids measured in a solar furnace ZrO2–TiO2 system. Sol. Energy, 1967, 11, 56–61.

65. Shevchenko, A. V., Lopato, L. M., Maister, I.M. and Gorbunov, O. S., Russ. Inorg. Chem. (Engl. Transl.), 1980, 25, 1379–1381.

66. Ono, A., Miner. J., 1972, 6, 433–441.

67. Valtera, Jan & Kalous, Tomáš & Pokorny, Pavel & Batka, Ondrej & Bílek, Martin & Chvojka, Jiri & Mikes, Petr & Kostakova, Eva & Žabka, Petr & Ornstova, Jana & Beran, Jaroslav & Stanishevsky, Andrei & Lukas, David. (2019). Fabrication of dual-functional composite yarns with a nanofibrous envelope using high throughput AC needleless and collectorless electrospinning. Scientific Reports. 9. art.#1801. 10.1038/s41598-019-38557-z.

68. Aaron M. Drews, Ludovico Cademartiri, Michael L. Chemama, Michael P. Brenner, George M. Whitesides, and Kyle J. M. Bishop Phys. Rev. E 86, 036314 – Published 20 September 2012

69. Electric Winds Driven by Time Oscillating Corona Discharges A. M. Drews, L. Cademartiri, G. M. Whitesides, K. J. M. Bishop* Journal of Applied Physics 2013, 114, 143302

70. Taylor, G. I., Electrically driven jets. Proceedings of the Royal Society of London A 313, 453 (1969).

71. Taylor, J. R. M. a. G. I., Electrohydrodynamics: A review of the role of inerfacial stresses. Annu. Rev. of Fluid Mech 1, 111 (1969).

72. Moses M. Hohman, M. S. G. R. M. P. B., Electrospinning and electrically forced jets. I. Stability theory. Physics of Fluids 13 (2001).

73. Saville, D. A., Electrohydrodynamics: The Taylor-Melcher leaky dielectric model. Annual Review of Fluid Mechanics 29, 27 (1997).

74. Saville, D. A., Electrohydrodynamics stability: Fluid cylinders in longitudinal electric fields. Phys. Fluids 13, 2987 (1970).

75. Saville, D. A., Stability of electrically charged viscous cylinders. Phys. Fluid Mech. 49, 361(1970).

76. Mestel, A. J., Electrohydrodynamic stability of a slightly viscous jet. J. Fluid Mech. 274, 93(1994).

77. J. M. Lopez-Herrera, A. M. G.-C. a. M. P.-S., One dimensional simulation of the breakup of capillary jets of conducting liquids: Applications to e.h.d. spraying. J. Aerosol Sci 30, 895(1999).

78. R. Kessick, J. F. G. T., The use of AC potentials in electrospraying and electrospinning processes. Polymer 45, 2981-2984 (2004).

79. W.M. Groenewoud, chapter 2 - Thermogravimetry, Editor(s): W.M. Grounewoud, Characterization of Polymers by Thermal Analysis, Elsevier Science B.V., 2001, Pages 61-76, ISBN 9780444506047

80. Jiji Abraham, Arif P. Mohammed, M.P. Ajith Kumar, Soney C. George, Sabu Thomas, Chapter 8 - Thermoanalytical Techniques of Nanomaterials, Editor(s): Sneha Mohan Bhagyaraj, Oluwatobi Samuel Oluwafemi, Nandakumar Kalarikkal, Sabu Thomas, In Micro and Nano Technologies, Characterization of Nanomaterials, Woodhead Publishing, 2018, Pages 213-236, ISBN 9780081019733, https://doi.org/10.1016/B978-0-08-101973-3.00008-0.

81. Bhadeshia H.K.D.H. "Thermal analyses techniques. Differential thermal analysis". University of Cambridge, Material Science and Metallurgy. www.msm.cam.ac.uk/phase-trans/2002/Thermal1.pdf

82. Berger K.G., Akehurst E.E. "Some applications of differential thermal analysis to oils and fats". International Journal of Food Science & Technology, 1966, 1, 237–247.

83. Smykatz-Kloss W., Heil A, Kaeding L. and Roller E. "Thermal analysis in environmental studies". In: Thermal analysis in Geosciences. Springer Berlin / Heidelberg, 1991.

84. Goldstein, G. I. et al., Scanning electron microscopy and x-ray microanalysis. Plenum Press (1981).

85. Suzuki, E., High-resolution scanning electron microscopy of immunogold-labelled cells by the use of thin plasma coating of osmium. J. Microscopy 208, 153-157 (2002).

86. Frank, A., The Cambridge Structural Database: a Quarter of a Million Crystal Structures and Rising. Acta Crystallographica Section B 58, 380-388 (2002).

87. Askeland, D. R. & Phulé, P. P., The Science and Engineering of materials, 5th ed. (CengageLearning, 2006).

88. J. Wittke, "Secondary Electron Imaging." http://www4.nau.edu/microanalysis/Microprobe/Imaging-SEM.html (Accessed May 2, 2007).

89. W. Bigelow, Introduction to the Scanning Electron Microscope (University of Michigan, 2004).

90. Joseph Goldstein (2003). Scanning Electron Microscopy and X-Ray Microanalysis. Springer. ISBN 978-0-306-47292-3.

91. Cullity, B. D., Elements of XRD, 2nd ed. Addison-Wesley, Reading, MA, USA, (1978).

92. Rietveld, H. M. (2 June 1969). "A profile refinement method for nuclear and magnetic structures". Journal of Applied Crystallography. 2 (2): 65–71.
93. Pecharsky, Vitalij K. Fundamentals of Powder Diffraction and Structural Characterization of Materials. ISBN 9780387095790. OCLC 690510145.

94. Speakman, Scott A. “Fundamentals of Rietvield Refinement.” Fundamentals of Rietvield Refinement , MIT, 2011, prism.mit.edu/xray/Fundamentals%20of%20Rietveld%20Refinement%20XRD%20Simulation%202011.pdf.

95. Saenko, I., Ilatovskaia, M., Savinykh, G., Fabrichnaya, O. Experimental investigation of phase relations and thermodynamic properties in the ZrO_2–TiO_2 system(2018) Journal of the American Ceramic Society, 101 (1), pp. 386-399.

96. Bhaskar, S., Park, J.G., Lee, K.S., Kim, S.Y., Kim, I.J., Thermal and mechanical behavior of $ZrTiO_4$-TiO_2 porous ceramics by direct foaming, (2016) Ceramics International, 42 (13), pp. 14395-14402.

97. Kim, I.J., Lee, K.S., Cao, G., Low thermal expansion behavior of $ZrTiO_4$-Al_2TiO_5 ceramics having high thermal durability between 750 and 1400°c, (2002) Key Engineering Materials, 224-226, pp. 819-824.

98. Polliotto, V., Albanese, E., Livraghi, S., Agnoli, S., Pacchioni, G., Giamello, E. Structural, electronic and photochemical properties of cerium-doped zirconium titanate (2018) Catalysis Today, Article in Press.

99. Kim, I.J., Gauckler, L.G., Formation, decomposition and thermal stability of Al_2TiO_5 ceramics (2012) Journal of Ceramic Science and Technology, 3 (2), pp. 49-60.

100. Bannister, M.J. and Barnes, J.M. (1986), Solubility of TiO_2 in ZrO_2. Journal of the American Ceramic Society, 69: C-269-C-271.

101. Troitzsch, U. (2006), TiO_2-Doped Zirconia: Crystal Structure, Monoclinic-Tetragonal Phase Transition, and the New Tetragonal Compound Zr_3TiO_8. Journal of the American Ceramic Society, 89: 3201-3210.

102. Helfried Näfe and Devendraprakash Gautam. Metastable Nanocrystalline Zirconia in Light of the Nucleation Theory. The Journal of Physical Chemistry C 2016 120 (19), 10523-10529

103. Basnet, B., Sarkar, N., Park, J.G., Mazumder, S., Kim, I.J., Al_2O_3–TiO_2/ZrO_2–SiO_2 based porous ceramics from particle-stabilized wet foam, (2017) Journal of Advanced Ceramics, 6 (2), pp. 129-138.

104. Dutta, H., Nandy, A., Pradhan, S.K., Microstructure and optical characterizations of mechanosynthesized nanocrystalline semiconducting $ZrTiO_4$ compound, (2016) Journal of Physics and Chemistry of Solids, 95, pp. 56-64.

105. Bhaskar, S., Park, J.G., Kim, I.J., Kang, B.H., Lim, T.Y.
$ZrTiO_4$ porous ceramics fabricated from particle-stabilized wet foam by direct foaming (2016) Journal of the Korean Physical Society, 68 (1), pp. 77-82.

106. Rendtorff, N.M., Gómez, S., Gauna, M.R., Conconi, M.S., Suarez, G., Aglietti, E.F. Dense mullite-zirconia-zirconium titanate ceramic composites by reaction sintering (2016) Ceramics International, 42 (1), pp. 1563-1572.

107. Zhu, L., Liu, B., Qin, W., Liu, H., Lin, X., Cai, N., Wang, X., Xu, D. Oriented and ordered mesoporous ZrO_2/TiO_2 fibers with well-organized linear and spring structure (2015) Materials Research Bulletin, 68, pp. 216-220.

108. Donfeu Tchana, R., Pfeiffer, T., Rüdinger, B., Deubener, J., Spectroscopy study on the nucleation kinetics of ZrTiO4 in a lithium alumosilicate glass, (2014) Journal of Non-Crystalline Solids, 384, pp. 25-31.

109. Borrell, A., Salvador, M.D., Rocha, V.G., Fernández, A., Gómez, A., López-López, E., Moreno, R., ZrTiO4 materials obtained by spark plasma reaction-sintering, (2014) Composites Part B: Engineering, 56, pp. 330-335.

110. Wang, J., Cheng, J.-S., Deng, Z.-L., Effect of alkali metal Oxides on viscosity and crystallization of the MgO-Al2O3-SiO2 glasses, (2013) Physica B: Condensed Matter, 415, pp. 34-37.

111. Pramanik, S., Pal, S., De, G., Au nanoparticles doped $ZrTiO_4$ films and hydrogen gas induced Au-plasmon shifting (2010) Journal of Materials Chemistry, 20 (41), pp. 9081-9088.

112. Dutta, H., Pradhan, S.K., In-situ high temperature annealing of nanostructured $ZrTiO_4$ prepared by mechanical alloying
(2010) Physica E: Low-Dimensional Systems and Nanostructures, 42 (5), pp. 1772-1776.

113. Gajović, A., Šantić, A., Djerdj, I., Tomašić, N., Moguš-Milanković, A., Su, D.S., Structure and electrical conductivity of porous zirconium titanate ceramics produced by mechanochemical treatment and sintering (2009) Journal of Alloys and Compounds, 479 (1-2), pp. 525-531.

114. T. Miloh, B. S. A. L. Y., Needleless electrospinning: Electrically driven instability and multiple jetting from the free surface of a spherical liquid layer. J. Appl. Phys. 106 (2009).

115. D. Lukas, A. S. P. P., Self-organization of jets in electrospinning from free liquid surface: A generalized approach. J. Appl. Phys 103 (2008).

116. M. Shin, M. M. H. M. P. B. C. R., Electrospinning: A whipping fluid jet generates submicron polymer fibers. Appl. Phys. Lett 78, 1149 (2001).

117. Soshana A. Smitha, B. P. W. Y. L. J., Effect of polymer and ceramic morphology on the material and. J. Mem. Sci 526, 315-322 (2017).

118. Doshi J, R. D., Electrospinning process and applications of electrospun fibers. J. Electrostatics 35, 151-160 (1995).

119. C. Lawson, A. S. S. P. L., Rapid fabrication of poly(ε-caprolactone) fibers using needleless alternating current electrospinning. J. Appl. Polym. Sci. 133, 43232 (2016).

120. S. Maheshwari, H. C. C., Assembly of multi-stranded nanofiber threads through AC electrospinning. Adv. Mater 21, 349-354 (2009).

121. A. Stanishevsky, J. W. M. W. I. S. H. Y.-L., Ribbon-like structures of tungsten oxide nanofibers. RCS Adv. 5, 69534-69542 (2015).